Chapter 4
Functional Imaging of Cone Photoreceptors

Lawrence C. Sincich, Ramkumar Sabesan, William S. Tuten, Alexander Meadway, Austin Roorda, and Wolf M. Harmening

Abstract Color pervades our visual sensory world, yet our understanding of the neural basis of color perception, starting with the retina and on through the multiple cortical areas that subserve vision, is still incomplete. The L, M, and S cone photoreceptors, being the cellular entry point for trichromatic vision in humans and other primates, have been studied in a variety of ways to reveal their relative numbers, their spatial arrangement, and their anatomical connectivity. We review work in these species that has linked mapped cone mosaics directly to functional properties such as single neuron responses in the retina and color percepts arising from cone-targeted microstimulation. We also highlight important technical issues that constrain access to single cone photoreceptors for functional studies.

Keywords Cone photoreceptors · Waveguides · Adaptive optics · Absorptance imaging · Optoretinography · Microstimulation · Chromatic dispersion · Fixational eye motion · Retinal vessels · Increment threshold · Dysflective cones · Color psychophysics

L. C. Sincich (✉) · A. Meadway
Department of Optometry and Vision Science, University of Alabama at Birmingham, Birmingham, AL, USA
e-mail: sincich@uab.edu

R. Sabesan
Department of Ophthalmology, University of Washington, Seattle, Washington, USA

W. S. Tuten · A. Roorda
Herbert Wertheim School of Optometry and Vision Science, University of California, Berkeley, CA, USA

W. M. Harmening
Department of Ophthalmology, University of Bonn, Bonn, Germany

J. Kremers, R. C. Baraas (eds.), *Human Color Vision*, Springer Series in Vision Research, https://doi.org/10.1007/978-3-032-09457-5_4

4.1 Introduction

That the world is a colorful experience for most of us is a consequence of two biological feats. One is that our retina has evolved distinct sets of photoreceptors and circuitry that preserve wavelength-specific sensitivities in the neural output signals sent to the brain. The other is that our visual cortex is able to elaborate upon those retinal inputs in a variety of enriching and advantageous ways. The confluence of these two feats is the foundation of color perception. For instance, the three primary categories of photoreceptors that populate the eye in humans arose through an evolutionary process that was neurally independent of the brain—as there are no known neural projections from the brain to the retina—yet it is clear that rather than ignoring the emergence of trichromatic capability, cortical processing took advantage of what the retina had to offer. Perhaps an extreme counterexample of this evolutionary point is found in mantis shrimp, which have 12 photopigments yet ended up with color discrimination that is limited to being trichromatic [1]. The aim of this chapter is to examine the handshake between the eye's photoreceptors and the brain, based on a variety of techniques, some very new, some time-proven, that are giving us fresh access to the cellular basis of color vision.

Our particular focus is on cone photoreceptors, how their spectral sensitivities can be identified in humans and other primates, and how their individual response properties can be studied at the perceptual level. Assessing percepts at the cellular level is a special challenge because cones are undeniably small. Depending on the individual, cone inner segment diameters can be 1.5–2 μm at the foveal center, though they increase in size rapidly with eccentricity, reaching a typical diameter of 6–8 μm that nearly plateaus at about 5° eccentricity from the fovea [2, 3]. Cone inner segment diameter is commonly used as the anatomical determinant of photoreceptor size because it sets a primary optical constraint on light capture. To study such small cells individually, microscopic access is required. As we will see, an extensive body of work has used retinal tissue removed from the eye and kept physiologically maintained in vitro for functional studies at the cellular scale. Developments in ocular imaging now provide direct microscopic access to cones in vivo [4, 5] and have continued to improve over the last decade, paving the way for combined biophysical and psychophysical studies of single cones as it relates to color vision in the living eye.

4.2 Optical Constraints on Imaging Cones

Before beginning our survey of functional cone imaging, it is important to appreciate a few of the technical constraints that shape the experimental strategies used for studying cones. This section is necessarily brief given the long history of the issues, but comprehensive references are provided.

4.2.1 Photoreceptor Waveguiding

In order to see the photoreceptors at the microscopic scale in an intact eye, a beam of light is usually projected onto the retina and the reflected light is detected by some means. It is useful to realize that only about 1% or less of the light entering the eye is reflected back out, with the exact percentage being dependent on wavelength [6]. The remainder is either scattered or absorbed by tissues, and of the latter only a fraction is actually captured by the photopigments that allow us to see [7]. For example, of just the light that enters a cone's inner segment, it has been estimated that about 30% is absorbed by photopigment [8]. For the 1% of the light that is reflected back from the eye, this occurs in part because the somewhat planar tissue of the retina acts like a weak mirror, having a very noticeable directional component. Much of this direction-dependency is due to the fact that photoreceptors act like optical waveguides, able to funnel light efficiently along their length [9–12] (but see [13] for an alternative theoretical interpretation). At the scale of individual photoreceptors, it has become increasingly appreciated that multiple reflective surfaces within a single cone exist, enabling phase-dependent changes in reflected light to be measured in the living eye (detailed in Sect. 4.3).

Once light enters the cone inner segment, internal reflections channel the light down the long axis of the cell. This has several consequences. One is that light is captured more efficiently than if there was no waveguiding, because it can be collected over a broader range of beam positions and angles. Light entering straight into the face of the inner segment has the best chance of being captured by the photoreceptor, unsurprisingly, while light hitting the face at increasing larger angles can still be captured, though with decreasing effectiveness. The light coupling efficiency is a two-dimensional function of the angle of light entry and can be pictured as having an approximately Gaussian shape. This angular sensitivity of light capture can be measured perceptually in a variety of ways (referred to as the Stiles-Crawford effect [14–16]), one of which leads to an estimate of the dimensions of the light capture profile for single cones [17, 18]. For light heading into the eye, waveguiding helps it to be absorbed more readily by cone outer segments where the photopigments reside, as the walls of the funnel-shaped inner segment direct light towards the entrance of the outer segment (Fig. 4.1).

Waveguiding is equally effective for light reflected back through the photoreceptor, since optical systems are reversible. The cones themselves are now considered to have several reflective structures concentrated at two sites: the anatomical junction between the inner and outer segment, and the junction between the outer segment and its contact with retinal pigment epithelium [19–22]. Thus, a second consequence of waveguiding is that when light hitting these junctions is scattered, internal reflections can direct some of this light back along the path of the entering light; this portion would otherwise be lost if simply coming off a scattering surface. Such a waveguide effect is good news for cone imaging based on reflectance, as it leads to peaks of light intensity that approximately correspond to the center of each photoreceptor (Fig. 4.2). As we shall see in the next sections, the pointillism of retinal reflection allows each photoreceptor to be identified and returned to day after day for functional studies, when suitable methods are used.

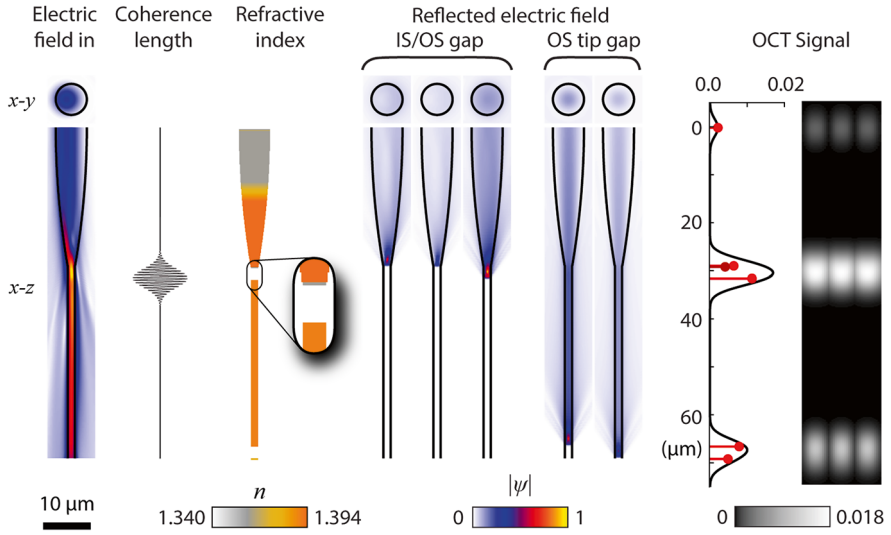

Fig. 4.1 Light propagation in cone photoreceptors is waveguided inward (left) and during reflection (middle panels) given the known refractive indices shown in this model of a single cone under AO imaging conditions. Where there is an abrupt change in refractive index, the magnitude of the reflected light is calculated and propagated back up the receptor. The resulting power of the light at a detector is shown, taking into account interference effects. Interference can also occur if the reflectors lie within the coherence length of an imaging source. In this example we show the envelope that indicates the magnitude of the interference of a 10 μm coherence length source. With this source, reflections from the IS/OS gap do not interfere with those from the OS tip. OCT can be simulated (right) by convolving the square root of the power of reflections with a Gaussian (here coherence length = 4.2 μm). The OCT image shows a beam being scanned across 3 cones. (Adapted from [19])

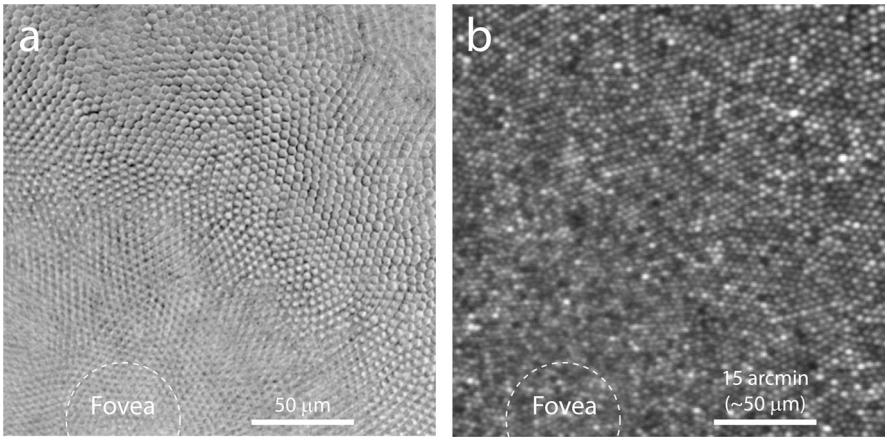

Fig. 4.2 Perifoveal mosaic of cone inner segments in a macaque retina. (**a**) *En face* view of a flattened unstained macaque retina, imaged with phase-contrast microscopy. Because the length of the inner segments increases rapidly just outside the foveal center (dashed line), only an arc of them are in sharp focus at the level of the inner limiting membrane. Also evident is the increase in inner segment diameter with distance from the fovea. (**b**) Adaptive optics image taken in vivo of the same region of retina from a different macaque eye. Most cones in the mosaic are well resolved, except within ~30 arcmin of the fovea, where the reflectance image is compromised by patterns arising from light interference. Imaging wavelength = 710 nm

4.2.2 Use of Adaptive Optics Technology for In Vivo Imaging

While waveguiding is a helpful optical property of cones—both for improving a cone's light capture and for making retinal imaging easier—it still remains a technical challenge to image cones at the microscopic scale in vivo. Under a limited set of circumstances in humans, individual cones can be seen using the natural optics of the eye [23–26]. But to attain diffraction-limited imaging of cones with wide fields of view, to achieve this in most subjects, and to do so in real-time as is needed for psychophysical testing, a method for rapidly measuring and correcting the normal optical aberrations of the eye is necessary. Beginning in the 1990s, the first practical means of making optical aberration correction for human eyes brought such imaging within reach (reviewed in [4, 27]). The method entails two main features: a wavefront sensing device to measure the ocular aberrations, and a deformable mirror that can compensate for those aberrations. Devices using such approaches add the term adaptive optics (AO) to the instrument name because the wavefront measurements and compensations are updated regularly to accommodate aberration changes that are constantly occurring in the living eye [5, 28].

Ophthalmoscopes that have used AO for imaging the retina at high resolution are now generally configured in one of three ways. The first was a flood illuminated system, using a flash of light and a CCD camera to create single full-frame images [29]. The second used a raster-based scanning laser system to create a continuous stream of images that could be easily recorded as a movie [30]. The third and newest design is also raster-based but uses optical coherence tomography (OCT) as the underlying technique [31]. Each of these systems has advantages and disadvantages with respect to studying human color vision. Flood AO systems are optimal for capturing an instantaneous retinal image that is nearly free of distortions due to eye movements. Because of this, they have been used extensively for absorptance imaging of the cone mosaic (described below). Wavefront correction, however, has been time consuming with flood systems, and the retinal locus of any stimulus delivery is uncertain at the cellular scale. AO-based scanning laser ophthalmoscopes (AOSLOs) enable rapid wavefront correction and tracking of stimulus delivery locations, but the unavoidable eye motion distortions require extensive effort to overcome. To the degree that they have been overcome—as we will detail later in this chapter—AOSLO systems are able to probe color vision at the individual cellular level because stimuli can be delivered through the same optical path taken by the imaging light. Combining AO with OCT systems yields a wealth of imaging data through the depth of the retina (due to the high z-axis resolution), but it currently has limitations on the kind of stimuli that can be presented for testing vision and image resolution at the foveal center.

4.3 Biophysical Cone Imaging

A very substantial literature exists on the biophysical characterization of cone photoreceptors, beginning with spectrometric studies of the isolated photopigments [32, 33] to the electrophysiological characterization of spectral sensitivity functions measured via photocurrents [34]. In this section, we will limit ourselves to experiments that have drawn on imaging approaches to answer questions specific to intact retinas. What proportion of the retina is occupied by each cone class? Do these proportions vary between individuals? Are the cones randomly arranged? Is there regional variation in cone composition across the retina?

Because cone photoreceptors have broad sensitivities to wavelengths of light, they are usually referred to by their long, medium or short wavelength peak sensitivities: L cones (traditionally associated with "red" signaling), M cones ("green"), and S cones ("blue"). Although it is discussed in detail elsewhere in this book (see Chap. 3), we note here that the peak sensitivities of three cone classes can differ depending on how they are measured. For macaque cones measured electrophysiologically, the peak wavelength sensitivities are L cones = 561 nm, M cones = 531 nm, and S cones = 430 nm [34, 35]. Because these values agree reasonably well with physiological and microspectrophotometric values obtained from human L and M cones [36–40], as well as psychophysically measured sensitivity peaks when derived from a nomogram fit (Eq. 8 of [41]), we will use these peak sensitivity values in this chapter without adding further qualifications.

4.3.1 Absorptance Classification of Cones In Vitro

One of the earliest in situ maps of L, M, and S cones was made by applying microspectrophotometric methods developed for use in isolated photoreceptors [42, 45] to classify cones in a piece of flattened retinal tissue (Fig. 4.3a). This revealed a mosaic that appeared to have a random distribution of L and M cones, although the mapped set of cones was perhaps too small to learn definitively if cones of like type were non-randomly clustered together. The method required the cones to be measured one at a time, limiting the number that could be studied. Shortly after, a video-based method was devised to measure differential photopigment bleaching over an entire microscopic field of view in one pass (Fig. 4.3b). This yielded a non-random arrangement of L and M cones [8]. At the time of these studies, the distribution of S cones had already been shown to be fairly regularly distributed across the retina, except in the foveola where they are absent, using histochemistry or antibodies to the S cone opsin [46–49]. With no antibody available that can distinguish between L and M cones, imaging based on differential absorption of spectral light remains the primary biophysical means for mapping the cones by class. By the mid-1990s, with only a few small cone maps available, any order in the spatial arrangement of L and M cones still remained an open question.

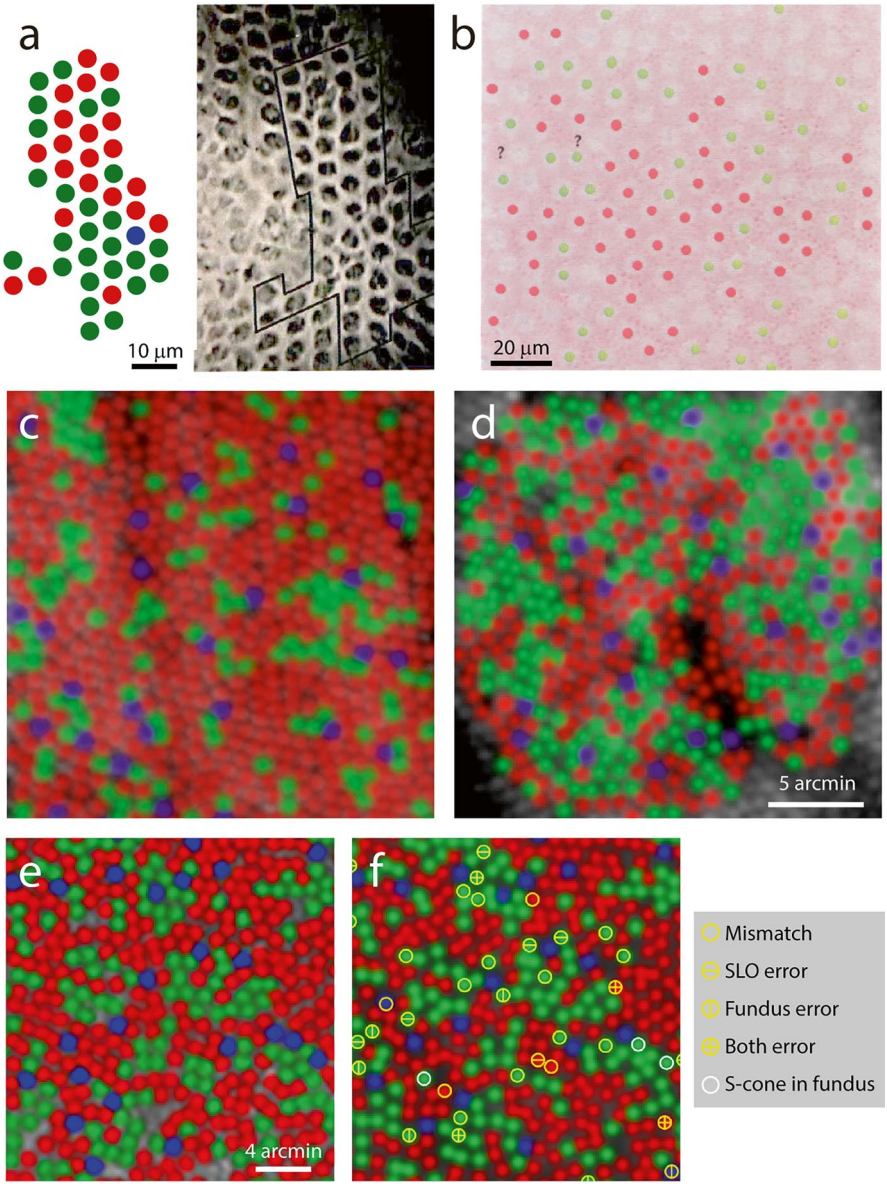

Fig. 4.3 Photopigment absorptance imaging of the trichromatic cone mosaic. L, M, and S cones are represented by red, green, and blue, respectively, in all panels. (**a**) Microspectrophotometric mapping of cones from a freshly dissected talapoin foveal retina. (Adapted from [42]). (**b**) Photopigment transmittance mapping in an excised macaque peripheral retina. Candidate S cones are indicated by a question mark to the left. (Adapted from [8]). (**c, d**) Pseudocolor images of the cone mosaic in two human subjects, mapped in the living eye via differential photopigment bleaching in conjunction with AO imaging. Retinal areas are 1° from the fovea. Statistical analysis showed a random distribution of L and M cones in **c**, and a non-random distribution in **d**, though it may have arisen from optical blur in this subject. (Adapted from [43]). (**e, f**) Pseudocolor images of the same patch of retina in one subject classified with AO fundus imaging in **e** and with AOSLO in **f**. Only a small number of possible misclassifications were found. (Adapted from [44])

Why is it important to know the distribution of L and M cones? The main reason has been to learn how color signals are initially established. For a color signal to be perceived within the red-green portion of the spectrum, there must be a comparison at the neural level between activity arising from L cones versus M cones. Such L/M opponency is generally considered to be established via receptive field center/surround antagonism, and transmitted by midget retinal ganglion cells to the rest of the brain [50] (also see Chap. 5). Since these ganglion cells appear to receive inputs from all the cones lying within their dendritic field [51–57], a purely random arrangement of L and M cones would often lead to nearly equal L and M drive between receptive field centers and surrounds, producing an achromatic signal. If, however, L and M cones had non-random distributions, the centers and surrounds would more likely manifest differences in L and M composition, thereby producing a chromatic signal.

The foregoing assumes that many cones subserve the receptive field center and surround, which is the case in the retinal periphery. As one moves closer to the fovea, the receptive field sizes get smaller, and consequently, the cone composition of the receptive field centers is more likely to be of a single class if the cones are arranged non-randomly. To confer a color signal near the fovea, therefore, the field surrounds must receive input from cones of the opposite type from those in the field center. There has been a controversy over the purity of the cone composition in the surround. Some physiological studies have concluded that field surrounds of most cells are cone pure [58–61]. Others have found that surrounds can have varying degrees of mixed cone inputs [62–65]. Without knowing the cone composition of the individual receptive fields recorded, these mixed results could be attributed to either random or non-random cone arrangements, or to varying ratios of L and M cones. Unraveling this dilemma is essential for understanding color vision because these midget ganglion cells also carry the highest spatial information and represent more than 80% of all ganglion cells in the retina [66, 67]. Definitive mapping of the cone mosaic would help to clear up the functional role of this important cell class.

4.3.2 Absorptance Classification of Cones In Vivo

The chance to classify larger fields of cones was created with AO-based imaging of the retina, where it became possible to examine hundreds of cones simultaneously in an intact eye. Differential absorptance imaging was first used in humans [43] (and later in a macaque [68]) where it was determined that the L and M cone distributions appeared random and had varying ratios between individuals (Fig. 4.3c, d). The extent of the variation in L:M cone ratio was confirmed and expanded in a later study of a larger population of human retinas [69]. The L:M cone ratio varied from 1.1:1 to 16.5:1 in this group of male subjects with normal color vision, with a median ratio of about 1.9:1. Interestingly, statistical analysis of the spatial

arrangement of the cones found that 5 of the subjects had randomly dispersed L and M cones, whereas the remaining 3 subjects had non-random arrangements, with 2 of these having significant local clustering of cones of like type. In one retina, the mosaics examined from opposite sides of the fovea had different L:M cone ratios (1.24:1 and 1.77:1). There is also a notable increase in the relative proportion of L cones with distance from the fovea [70]. Cone classification can be performed with either AO fundus or AOSLO imaging, with relatively good agreement when the same retina is studied (Fig. 4.3e, f) [44]. With many individual cone mosaics now classified, the picture that has emerged from this data—as it so often happens in biology—is that the phenotypes of cone arrangements are truly mixed. The L and M cone distributions can be random or non-random, and will very much depend on both subject and retinal locus.

What does this mean for color vision studies? Functional tests that use small chromatic stimuli will be most affected. If stimuli are to be targeted to small regions of cones, it will be questionable to rely on assumptions about L and M cone ratios or local spatial distributions. The variation in these factors will impact certain types of experiments: the relative efficiency of detecting spectral differences in small spots [71–75], the appearance of briefly flashed spots [76–80], the role of spot size, intensity, and eye movements in detecting color [81], hyperacuity derived from stimuli with chromatic differences [82, 83], the appearance of high-spatial frequency gratings (both chromatic and achromatic) [84, 85], and, in physiology, the spectral responses of neurons in the early visual pathways [86, 87]. The use of AO-imaged cone mosaics in conjunction with functional testing has already begun to firm up our insights about how percepts are shaped by the specific cones being stimulated [88], and as we'll see later in the chapter, this work is continuing.

That the cone mosaics classified via imaging in vivo actually do align with a physiological measure has been shown empirically. Heterochromatic flicker photometry has been used extensively to estimate L:M cone ratios [89, 90]. The idea behind the method is to flicker light combinations that drive either L cone or M cones in isolation, with the magnitude of the response under each condition being proportional to the number of L or M cones. Comparison of the AO imaging data with flicker-photometric electroretinograms (ERGs) in the same subjects found that variation in ERGs between subjects is well correlated with the L:M cone ratios [69, 91]. This result helps to explain the wide range of ERGs that are found even when photopigment spectra are known [92, 93]. However, there remains a discrepancy between the AO-derived L:M ratios and the ERGs, as the relationship is not unitary. The authors suggest that this may be due to a ~1.5-fold larger contribution to the ERG signal from each M cone versus each L cone [69], but the mechanism has not been identified. Even with a proportionality constant greater than 1, the good correlation between imaging data and ERG is a strong indicator that functional differences between individuals are keyed to specific L:M cone ratios.

4.3.3 Physiological Classification of Cones In Vitro

Biophysical imaging of cones is not limited to the photopigment absorptance approaches reviewed so far. There have also been many physiological studies that tap into the electrical responses following light stimulation to characterize retinal tissue. These methods provide opportunities to answer additional questions about retinal function that cannot be addressed by absorptance imaging. What is the cone composition of the receptive fields of neurons downstream from the cones? Is the functional weighting of each cone the same? How many different ganglion cells does each cone feed a signal to?

Much has been learned about the relative proportion of each cone type's input to the main cell classes found in the primate retina, using single electrode recordings combined with cell fills (e.g., bipolar cells [94], horizontal cells [95], ganglion cells [96]). In this section, however, we will focus on studies that have used imaging techniques in their experimental approach to cone function.

The first cones mapped physiologically were S cones [97]. Using a flat multi-electrode array, it was possible to record from many retinal ganglion cells simultaneously in a small piece of explant macaque retina while projecting a randomly flickering colored stimulus pattern onto the tissue. Given the spatial resolution of the stimulus and the relatively wide spacing of the S cones, the spike-triggered averaged responses of the blue-ON/yellow-OFF ganglion cells revealed an activity map of individual S cones. This functional map of a single cone class unveiled a few important themes that have since been demonstrated for all cone classes [98–100]. First, for a given ganglion cell, the functional strength of each cone providing input can differ markedly. For example, among six S cones that fed onto one blue/yellow ganglion cell, there was a nearly three-fold difference in excitatory input strength between cones (see Fig. 4a in [97]). Second, cones can provide input to more than one ganglion cell of the same type, suggesting that, at least in peripheral retina, receptive field centers can have some spatial overlap. Notably, when the same cone does connect to separate ganglion cells, the input strengths will differ to each ganglion cell. This indicates that there are genuine differences in synaptic strength from one cone to separate ganglion cells, rather than there being especially sensitive cones passing large signals to all downstream partners. Third, it was found that S cone signals combined linearly. Regardless of the relative activation of two S cones, the spiking output of the blue/yellow cell was a function of the summed input. In all of these ganglion cells, the yellow-OFF response, arising from combined L and M cone signals, was quantified, but the spatial resolution of the stimulus did not permit the mapping of individual cones. That resolution limit was overcome in a later study where mosaics of all three cone types were revealed in unprecedented functional detail for all of the major ganglion cell types [98]. Examples of complete cones maps for one ON and one OFF midget ganglion cell are shown in Fig. 4.4a. Each cone could be classified by the relative spike-triggered activity produced by the three color primaries of the stimulus display. Cones with ON responses appear as brighter values in these maps, while cones with OFF responses yield relatively

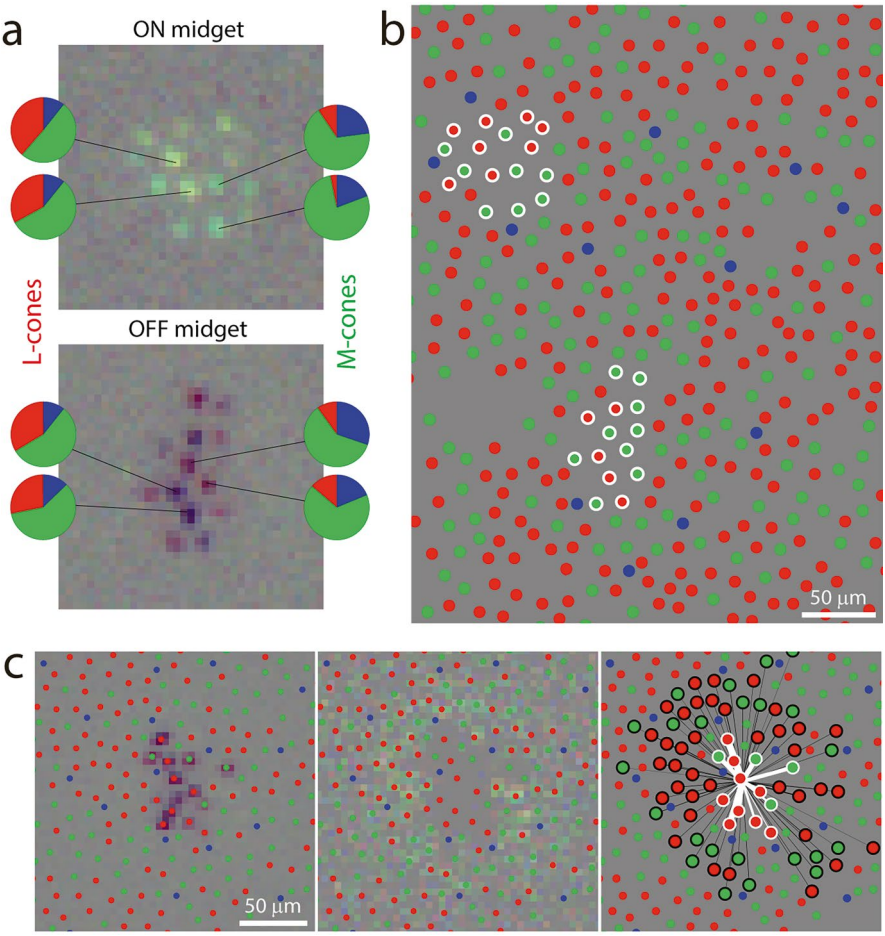

Fig. 4.4 Physiological cone classification and receptive field mapping of macaque retina in vitro. (**a**) The spectral sensitivity of cones providing input to the receptive field centers of two retinal ganglion cells is represented by the relative magnitude of the red, green, and blue pixel values in the image, each corresponding to spike-triggered average values (pie-diagrams). (**b**) For every cone in one recording, these values are converted into an index that discriminates L (red), M (green), and S (blue) cones. The cones identified from the retinal ganglion cells mapped in **a** are circled in white. (**c**) A cone mosaic from an OFF midget retinal ganglion, overlaid on normalized spike-triggered average maps, showing the strength of the cones defining the receptive field center (left) and surround (middle). A connectivity diagram (right), with line thickness proportional to the strength of each cone input, distinguishes the center response (white) from the surround (black, line thickness ×5 for visibility). (Adapted from [98])

darker values. As is evident in these maps of the receptive field centers, each cone can be unambiguously identified. The spike-triggered activity maps were confirmed to arise from individual cones anatomically, and each one has a different functional weight. In the set of eyes studied, the L:M cone ratio was 2:1, as had been estimated from previous macaque studies, and the S cones were 8% of the total population.

Because an entire array of cones was mapped simultaneously by recording from almost every ganglion cell in the field, it was possible to create not only a nearly complete mosaic of cones (Fig. 4.4b), but also to define the underlying functional connectivity between cones and ganglion cells. Cones supplying input to a receptive field center had the largest influence on ganglion cell spiking—as expected—while cones serving the field surround had much smaller weights of opposing magnitude (Fig. 4.4c). Complete sets of such connectivity diagrams for the ON and OFF varieties of both midget and parasol ganglion cells characterized several features of wiring specificity. One is that every cone provides input to each major ganglion cell class. This finding was later confirmed with single cone stimulation in vitro [99]. This means that sampling of the cone mosaic by each cell type is without gaps, and as a consequence, the visual field is represented contiguously by each ganglion cell type. In some instances, along the borders between the cone fields of ganglion cells, cone inputs are shared, indicating a slight overlap in the tiling of receptive fields. Another feature is that S cones provide input to more than just small bistratified ganglion cells [101]. About 10% of midget and parasol ganglion cells also sample from S cones, with the exception that about 60% of OFF midget cells receive input from at least one S cone. Therefore, S cone signals appear to be transmitted, in varying degrees, by all of the major ganglion cell types in macaque retina.

A third feature revealed in these data is how the cone composition of midget ganglion cell receptive fields undergirds L/M cone opponency, an issue that has been controversial [96]. Quantifying the relative strength of the L and M cone inputs, it was found that the midget ganglion cells exhibited red-green color opponency more often than predicted by random sampling. A statistical analysis of the number of L and M cones composing the field center and surround further showed that cones within the field center significantly favored connections of like type, whereas connectivity appeared random with cones in the surround. The bias in cone types for field centers was not due to cones of the same type being clumped together (as is occasionally seen in human retinas; see above). Instead, the cone opponency arose from more frequent connections of ganglion cells to cones of similar type, in addition to a stronger weighting of the same cones.

In summary, in vitro studies have offered exquisitely detailed information about cone function in the retina. Cones provide divergent and differently weighted inputs to all the major classes of ganglion cells, and there are connectivity biases that may boost red-green color perception, at least in the peripheral visual field. It appears that the features revealed so far are also present in central retina [102], where the cone weight variation and wiring specificity is likely to amplify color signaling in many cells. Functional cone mapping closer to the fovea is desirable in this regard, especially for in vivo work, and is the topic we move to shortly after covering a new method of characterizing cones.

4.3.4 Biophysical Functional Imaging of Cones In Vivo

Over the last 10 years, an entirely new approach to measure cone function has become available, one based on detecting the phase information of light reflected from the retina rather than intensity as used by absorption based methods. Collectively, these methods are termed optoretinography (ORG), indicative of their optical origin as a measure of cellular activity. Here we outline how these techniques have been used to quantifiably measure cone function.

The use of phase information in retinal imaging is a familiar one, as it is the basis for optical coherence tomography (OCT). When combined with adaptive optics, it enables three-dimensional imaging of individual photoreceptors. An OCT system using a spectrally broad source detects the light returned from the retina mixed with a reference beam. The signals from reflectors are encoded across the spectrum as modulations with frequencies proportional to the optical path difference between reflectors and the reference beam. A Fourier transform yields peaks at frequencies corresponding to the axial depth of reflectors, with amplitudes proportional to the square root of the reflectivity [103]. In addition, the signal contains phase information that can be used to detect any changes in the axial position of reflectors within a photoreceptor at the nanometer scale [104]. Although not widely appreciated, most neurons are subtly reshaped during physiological activity, and it is the detection of such morphological changes in cones that underlies all optoretinography methods [105–108].

With OCT optoretinography, photoreceptor outer segment length changes in response to a stimulus have been measured in frog and mouse rods [109, 110] and in human cones [111]. The phase responses that revealed outer segment lengthening were wavelength dependent and proportional to stimulus intensity. Stimuli with different wavelengths have been used with AOOCT to rapidly identify large numbers of individual cones as S, M or L [106, 112, 113] (Fig. 4.5a–d). There was a tight correspondence between absorptance and ORG cone classification when the same subjects were tested, with AOOCT classifying some cones that absorptance could not [114]. Phase sensitive OCT is also being applied to the study of eye disease, showing that disease progression can be monitored at the cellular level [115].

It is important to recognize that outer segment length changes are dynamic and bidirectional. There is an initial fast contraction followed by much slower dilation after a light flash (Fig. 4.5e, f). The slow dilation can last seconds, depending on stimulus intensity, extending the outer segment by up to 0.5 μm for bright stimuli. In contrast, the fast contraction has a consistent minima occurring at ~7 ms, with its amplitude dependent on stimulus intensity until saturation at ~40 nm [106]. This brief contraction is likely due to electrostatic potential changes and surface tension in the disc membranes at the onset of phototransduction, while the slower dilation has been linked to osmotic swelling or proteins associated with phototransduction [107, 110]. It has also been suggested that a single protein (PDE6) docked between the disc membranes causes both the contraction and dilation [116].

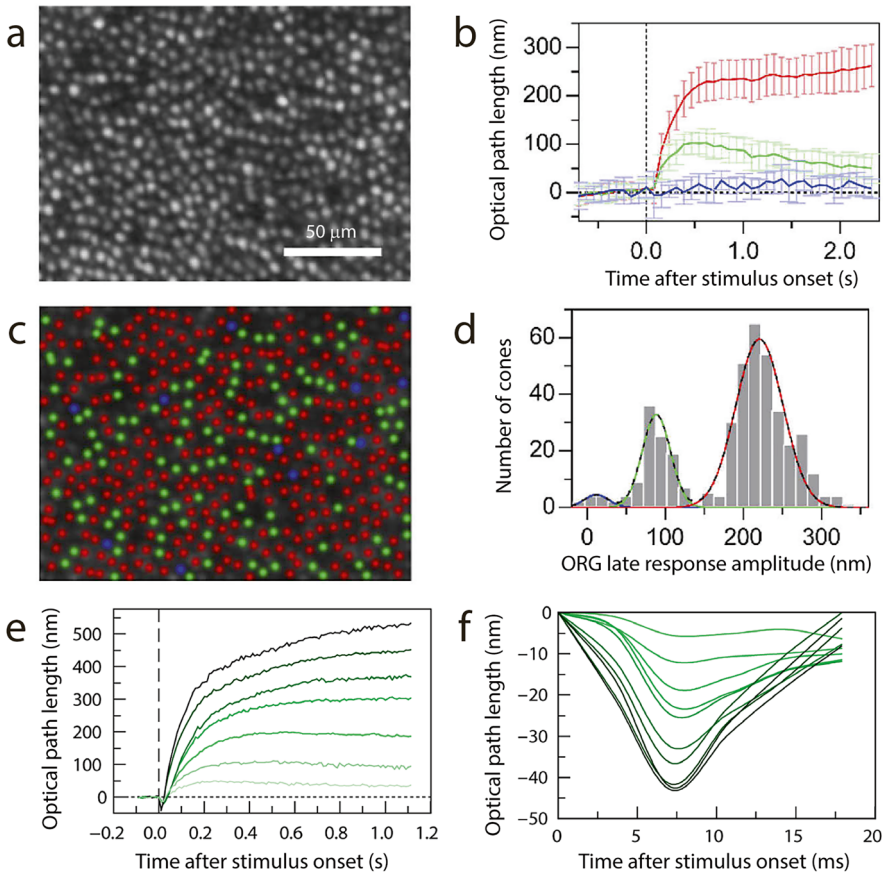

Fig. 4.5 Optoretinographic cone classification in the living human eye. (**a**) AOOCT image of cone photoreceptors at 4.75° eccentricity in temporal retina. (**b**) Outer segment optical path length increases measured after visual stimulation with 660 nm, showing mean signals (±1 SD) for L (red), M (green) and S cones (blue). (**c**) Classified cones for the image in **a**. (**d**) Histogram of ORG signal amplitudes show a clear peak for each cone class. (**e**) Late response ORG signals increase as a function of 528 nm stimulus intensity (range: 0.09–5.52 × 10^6 photons/μm^2, equal to 1.2–48.4% bleach). (**f**) Rapid initial ORG responses exhibit a brief outer segment contraction for lower stimulus levels (range: 0.04–1.82 × 10^6 photons/μm^2, equal to 0.4–18.5% bleach). (Panels **a–d** adapted from [112] and **e, f** from [106])

Optoretinographic signals can also be measured with an AOSLO, as images of cones change brightness in response to a stimulus in full field [117] or scanning systems [118]. The behavior appears like a scintillation, with individual cones becoming brighter, darker, or oscillating, all independently of one another [119]. On average, this change in reflected light tracks with stimulus intensity, follows the human luminosity function [120], and has a similar time course to the AOOCT late optoretinogram (Fig. 4.6). This signal has been used to sort cones into two groups

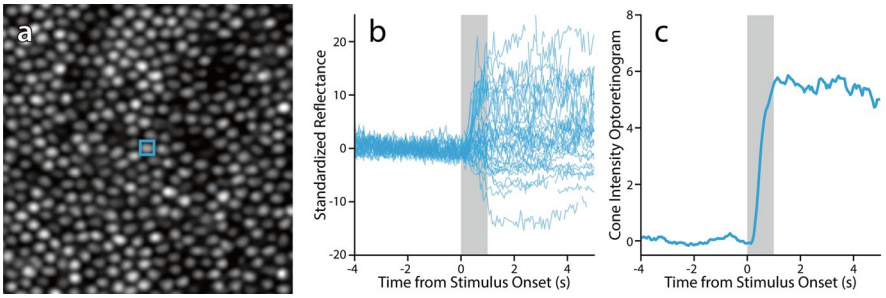

Fig. 4.6 ORG cone reflectivity changes with AOSLO imaging. (**a**) AOSLO image of cone photoreceptors at ~2° eccentricity, with cone analyzed outlined in blue. (**b**) Normalized changes in reflectance intensity over the selected cone after visual stimulation with 545 nm light (450 nW/deg^2), showing each trace from 48 trials. Stimulus epoch is shaded in grey. (**c**) Single cone ORG signal with a mean increase in reflected light. (Adapted from [121])

(S and L/M) using a 545 nm stimulus with good agreement to the absorptance method [121].

How can the amount of light reflected from cones change? An SLO measures the intensity of the light reflected from cones, a signal that includes the sum of all reflectors plus any possible interference effects. The effects of interference will be related to the optical path length differences between reflectors and the coherence length of the imaging light source. Thus when distances change between reflectors, as happens when the outer segment elongates, the summed reflected light will modulate. Such signals will go from a maxima to a minima with a change in the gap between reflectors of just a quarter wavelength, as the light from the reflectors shifts from being in-phase to out-of-phase.

The length of the outer segments varies with eccentricity but can be as long as 40 μm close to the foveal center [122]. This is an optical path length difference of ~80 μm, as the light from the deeper reflection makes a double pass. Scintillation is observed when using sources with longer coherence lengths than this (e.g., 95 μm in [121]). This may be attributable to the interference changing phase as the ends of the outer segment move further apart. However, interference effects have also been observed from light sources with coherence lengths less than 7 μm [119], while even shorter coherence lengths produce a smaller signal [118]. This suggests interference is also occurring between closely spaced reflectors, such as at the junction between inner and outer segments or between the outer segment tip and the retinal pigment epithelium, an idea which is consistent with the positions of prominent AOOCT signals from photoreceptors (Fig. 4.1). It is possible to isolate interference in AOSLO images of cones taken with short coherence lengths by subtracting images obtained with differing coherence lengths, so long as the center wavelength of the imaging sources are similar (Fig. 4.7). This is differential coherence imaging (DCI) [19], which can show movement of reflectors on the scale of a small fraction of a wavelength and holds promise for cone classification with visual stimulation.

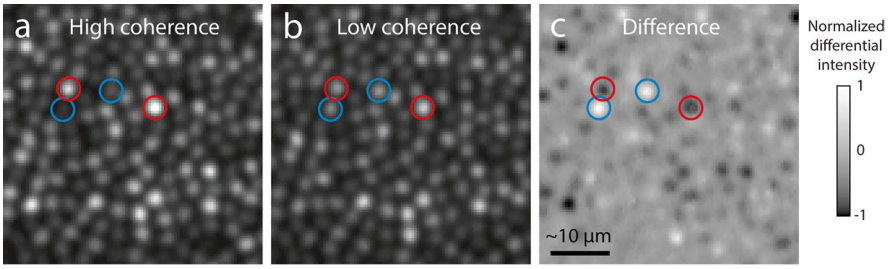

Fig. 4.7 Differential coherence images of cones. (**a**) AOSLO image at 1.7° inferior retinal eccentricity taken with light of coherence length = 14.7 µm. (**b**) Same retinal patch imaged light of coherence length = 4.8 µm. (**c**) Normalized differential coherence image (**b** minus **a**) illustrating the direction and magnitude of intensity changes caused by interference. Examples: negative DCI = red, positive DCI = blue. (Adapted from [19])

Optoretinography via OCT or SLO is becoming a useful tool not only for cone classification but more importantly for objectively studying cone function in vivo. By being able to detect nanoscale shape changes to photoreceptors in response to stimuli, we can attribute changes in photoreceptor state to phototransduction efficacy. Visual testing will no longer need to rely solely on perceptual reports, substantially expanding future investigations of normal and diseased cones at the cellular level.

4.4 Practical Constraints on Functional Cone Imaging In Vivo

Testing individual cones perceptually can lead to a number of insights about how cone signals are combined and ultimately generate color vision. With the advent of AO-based retinal imaging, investigators have begun to probe cones one by one for functional assessment. However, there are a number of technical challenges that any experimentalist needs to be aware of when testing vision at the cellular scale, especially with respect to color stimuli. In this section, we will delve into the more prominent hurdles that arise when trying to measure response properties that originate from one cone versus another.

4.4.1 Fixational Eye Motion

Vision testing with macroscopic stimuli can usually ignore the relatively small eye movements that occur during steady fixation, but when working at the cellular scale, the movements cannot be dismissed. Such eye motion has been classified into several varieties: typically microsaccades, tremor, and drift (reviewed in [123, 124]). It

suffices for the present purposes to simply emphasize that, even while actively fixating, a subject's eye is constantly moving. Most importantly, this motion is substantial when considering the cone mosaic, because a stimulus will be translated over many cones during even a brief bout of concentrated fixation (Fig. 4.8). To get a sense of the magnitude of this eye motion, a subject with good fixation (Fig. 4.8a) had a mean shift of 0.36 arcmin every 30 msec. If such shifts all went in one direction, as they sometimes do, this subject's drift would have moved a stimulus from one cone to its neighbor within 100 msec (this may be an overestimate, as the sampling rate for this data was low, 30 Hz, compared to other eye-tracking methods). Without continuous monitoring of eye position, and in the absence of microsaccades (rapid eye movements >2 arcmin), the only practical means of delivering stimuli to the same cone repeatedly is if stimuli are presented in rapid succession, less than 10 msec apart. Given the relatively slow photocurrent responses of cones, this will result in temporal summation and appear as a single stimulus [125, 126], limiting the utility of such a method. Because eye drift is akin to a random walk during any episode of fixation—sometimes directed toward areas with higher cone density for a given task [83]—stimuli presented over periods of time longer than 10 msec will frequently land on different cones. Video-based methods for tracking fixational eye motion in AO systems have been developed and are described below.

Eye motion is also present in anesthetized animals undergoing neuromuscular blockade, when the ordinarily suppressed cardiac and respiratory movement of the eye is released [127, 128]. Retinal motion under these conditions can occasionally be low, with excursions less than 10 μm, but this is still greater than the cone spacing in the fovea and perifovea (see Supplemental Fig. 2 in [129]). Thus, there is very little chance that a small stimulus presented at one location in visual space can land

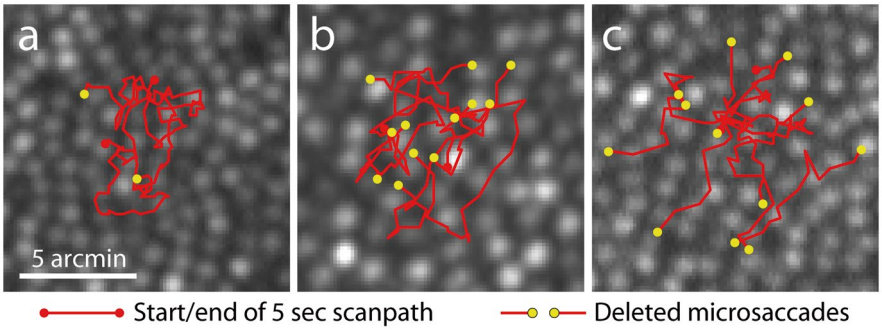

Fig. 4.8 Retinal motion in fixating subjects ranges over many cones. Each panel shows the cone mosaic and the reconstructed motion path from a 5 sec stabilized AOSLO movie recorded during active fixation at 30 Hz. Scanpaths (red) have had microsaccades deleted (yellow endpoints). Some subjects, as in (**a**), exhibit small frame-by-frame eye motion and rare microsaccades, while other subjects can have larger drifts and more saccades (**b**). Subjects can also manifest persistent drift along one axis, such as diagonal (**c**), with each drift canceled by a compensating microsaccade. As long as eye motion remains less than about one-third of the frame width (5× larger than these cropped images), video stabilization can track the position of cones targeted for stimulation. Eccentricities: **a** = 1.9°; **b** = 3.7°; **c** = 3.3°

on the same cone under any fixation condition, whether in humans or in animals with paralyzed eye muscles.

4.4.2 Chromatic Dispersion

From a purely optical standpoint, the performance of a normal eye is sometimes considered to be relatively poor, as the lens and cornea introduce high-order aberrations that interfere with high-resolution imaging, both spatially and temporally [29, 130]. Unlike defocus and astigmatism, the high-order aberrations cannot be eliminated with standard corrective lenses. As mentioned earlier, AO ophthalmoscopy has been fairly successful in ameliorating the distortions introduced by such aberrations, and presently enables imaging of both rod and cone photoreceptors in vivo [131, 132]. Once these aberrations have been corrected, there still remains the problem of chromatic dispersion. Simply put, a white point source of light will undergo dispersion by the ocular media and be projected onto the retina as a miniscule yet perceptible "rainbow," one with variably blurred colors. A means of accounting for chromatic dispersion of the eye is therefore a critical step. Without it, delivery of different wavelengths of light to a targeted location on the retina—at the micron scale of a single cone—is unfeasible. Such stimuli require chromatic correction because an infrared image is typically used as the reference image for AO correction, eye tracking, and target selection, whereas more visible wavelengths are used for stimulation. The shorter visible wavelengths have advantages especially for color vision studies: very high contrasts can be achieved, and wavelengths that optimally differentiate between cone types can be employed.

To correct for the chromatic dispersion of the eye, two optical parameters must be considered: longitudinal chromatic aberration (LCA) and transverse chromatic aberration (TCA). Multi-wavelength light originating from a single point will land on the retina with poor focus due to LCA, and in different locations because of TCA. It has been shown that LCA in the human eye is relatively consistent between individuals, and spans a substantial focal range [133–135]. For instance, the focal difference between a commonly used wavelength for imaging (840 nm) and a wavelength near the peak of visual sensitivity (540 nm) is 1 diopter, a value that translates to ~300 μm along the optic axis, a distance roughly equal to the thickness of the retina. Given this relationship (described by Eq. 5a in [134]), LCA can generally be corrected by appropriate static positioning of an instrument's optics for the wavelengths of interest, to bring them all into equal focus on the retina (Fig. 4.9a). It is worth noting that the LCA of some individuals may not fall on the population curve defined by Atchison and Smith [134]; one may wish to check for equal focus of imaging and stimulation channels by examining a retinal image containing a bipartite field of infrared and visible light.

TCA correction is more challenging because it depends on the position of the imaging beam relative to the pupil and to the achromatic axis of the eye [133, 137], and varies with retinal eccentricity [138]. Thus, for each experiment, TCA must be

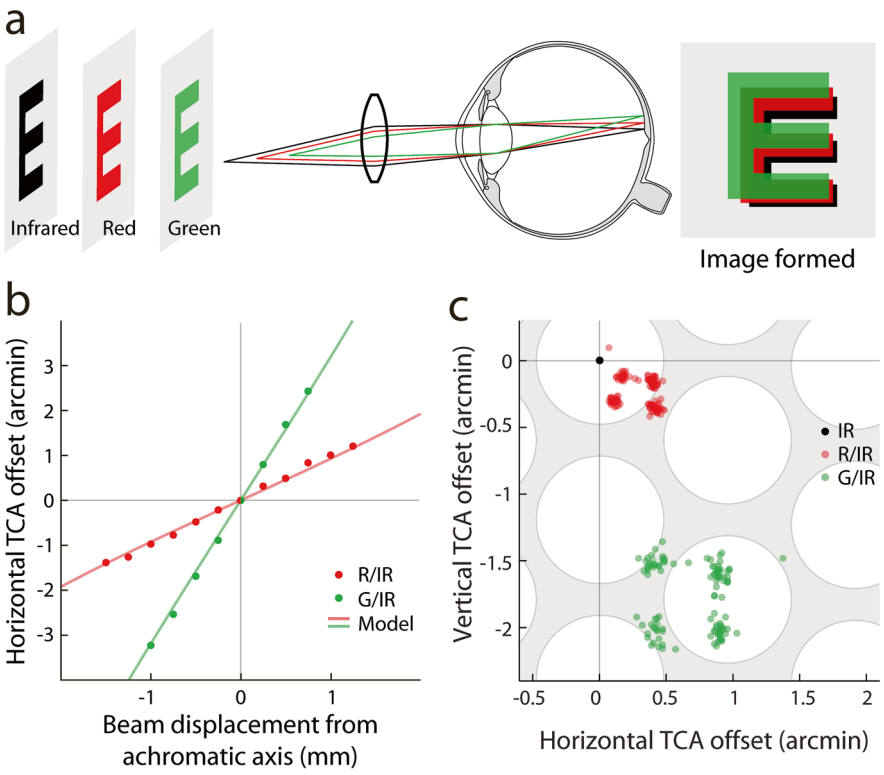

Fig. 4.9 Longitudinal and transverse chromatic dispersion in multi-wavelength retinal imaging. (**a**) Schematic of how longitudinal dispersion is corrected in an AOSLO, by setting different focal distances for each wavelength channel (computed according to [134]); this leaves transverse image offsets on the retina that must be measured and compensated. (**b**) Transverse chromatic offset measurements made from retinal imaging during horizontal pupil displacements (dots, means of 20 measurements) are compared to offsets computed from a standard chromatic eye model (lines). Pupil displacements of 0.25 mm produce offsets in the green channel that are more than twice the size of typical foveal cones (~0.4 arcmin). (**c**) Frame-by-frame measurements of transverse offsets (relative to an infrared channel, IR, at zero) during sequential fixation on four corners of a 1° square. Background circles represent 5 μm diameter cones. (Panels **b** and **c** adapted from [136])

corrected for a given pupil position and gaze direction. TCA is primarily caused by misalignment of the imaging beams relative to the eye's achromatic axis, along which TCA is zero by definition. However, finding the achromatic axis is difficult. It is known that the position of the achromatic axis relative to the pupil center is highly idiosyncratic, and so must be found empirically for every eye [139–141]. Instead of trying to pinpoint the achromatic axis and aligning all the beams to it, the problem can be solved more simply by measuring the offsets caused by TCA and beam misalignments in the resulting images directly [136]. Offsets measured this way are independent of the actual beam paths and the placement of the imaging detectors. Offsets are actually displayed on the retina, and are thus preserved as

spatial information in the acquired images. Measurement of TCA offsets from retinal images fits well with offsets calculated from a standard chromatic eye model (Fig. 4.9b). TCA can also be demonstrated for small gaze shifts on a frame-by-frame basis (Fig. 4.9c). In this illustrative example, if TCA was not corrected and a cone was selected in the infrared channel for stimulation with a green spot, the stimulus would have landed on a different cone, about 2 cone diameters away. Many of the cone-targeted studies cited in this chapter would not have been possible without the ability to correct TCA offsets.

Image-based TCA measurements have been validated psychophysically by comparing the offsets to a person's ability to assess small positional shifts of colored stimuli at the fovea [136, 142]. Because psychophysical thresholds in such tasks are lower than the sampling capacities of the cone mosaic (a perceptual feat usually called Vernier acuity or hyperacuity [133, 143]), chromatic offsets measured this way ought to match those calculated from an image-based approach. Such a match was found; the average difference between psychophysical and image-based TCA offsets was ~8 arcsec, equivalent to 1 pixel in the cone images [136]. This result shows that image-based TCA measurements are functionally identical to that of conventional subjective TCA measurements [133, 137, 144]. One notable advantage of an image-based method is that TCA can be measured in peripheral retina where subjective methods fail, because visual acuity is not precise enough outside the fovea. It is now clear that multi-wavelength light delivery onto single cones in the living eye hinges on measuring and correcting TCA rapidly and with good spatial fidelity, and leads to demonstrable benefits in visual tasks [141, 142]. To give the reader an idea of the scale of TCA effects, for each 1 mm beam shift at the pupil, there is about a 4 arcmin shift for green light [145], and TCA for a beam centered on the pupil changes by ~0.2 arcmin per degree of eccentricity [138].

4.4.3 Vascular Interference

When the eye is thought of as an electronic camera, the fact that blood vessels and capillaries cast a sinewy net over the photoreceptors is overlooked. Except in the small avascular zone centered on the fovea, the vessel beds can cover more than half of the inner retinal surface area [146–149]. These vessels can interfere with light capture and retinal imaging in different ways. One is simply by casting shadows. Ordinarily this passes unnoticed during everyday vision, much in the way that the 5° hole in the retina created by the optic nerve is not perceived. Such a visual scotoma can be probed easily to reveal the perceptual gap in the lateral visual field of each eye. Similarly, scotomas associated with large vessels coursing out from the optic nerve head can also be mapped, when probed with fine enough test spots [150, 151]. These angioscotomas have even been shown to modify the local circuitry in primary visual cortex [152, 153]. A direct test of how shadowing by small blood vessels can raise thresholds by at least a factor of 2 has been demonstrated with vessel-targeted microperimetry [154]. From all of this evidence, there is little doubt

that light being blocked by vessels perturbs the visual system at many levels, sometimes enigmatically so.

Shadowing is not the only form of light interference however. There is also light path distortion, arising from the clear cylindrical vessel walls and the pulsatile passage of blood cells through the narrow vessel lumen. These effects are more likely to operate on the scale of single cones. We and others, for instance, have noticed the transient alteration of reflected light from individual cones when a leukocyte passes over them [155–157]. Light reflecting back from a cone varies from bright to dark over time, and is sometimes displaced [158]. This is reminiscent of the blue-field entoptic effect that allows one's own retinal blood cells to be seen [159]. The irregular shapes of leukocytes, especially when squeezing through capillaries, make the effect of light path distortion unpredictable. Nonetheless, these light changes have been used to map out the anatomical position of the vessels themselves [160–162].

The development of phase contrast AOSLO imaging has highlighted how capillaries and various cells in the blood can alter the path of light impinging on the retina [119, 164]. The erratic and pulsatile movement of erythrocytes, leukocytes, and immune cells traveling through vessels showcases the dynamic nature of retinal blood flow [165, 166]. A comparison of cone reflectance against an overlying vascular map reveals not only the effect of shadowing, as many of the darkest cones are underneath vessel lumens, but also that some of the darker cones lie where the wall of the vessel—which is not seen in the vessel maps—may be steering light away from the imaging detection path (Fig. 4.10). Comparison of the two panels in this

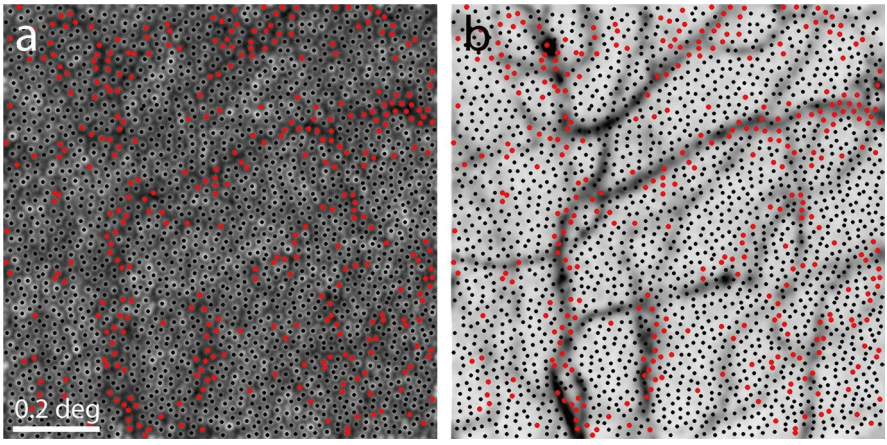

Fig. 4.10 Cones maps and retinal vasculature. (**a**) AOSLO cone image of a human retina, with gray levels scaled logarithmically to facilitate identification of poorly reflective cones. Cones brighter than the mean image reflectivity are marked with black dots (n = 1833), and those with reflectivity below the mean are indicated with red dots (n = 346). (**b**) Vasculature map derived from motion contrast imaging of same retinal area (but focused anterior to the cones) with cone centers from **a** superimposed, showing that most—but not all—dark cones are associated with blood vessels. Many other cones are situated under vessels but their reflectance is not appreciably affected. (Adapted from [163])

figure makes it evident that many of the capillaries are not apparent with the AO-corrected infrared light focused on the photoreceptor layer. As one might imagine, vascular interference can influence the functional imaging of cones, particularly if threshold measurements are of interest. The psychophysical testing described in the next section was conducted after first making vessel maps, thereby allowing cones to be selected for microstimulation where the potential hazard of light interference was minimized.

4.4.4 Characterization of Delivered Microstimuli

As with any optical device, diffraction will limit the spatial resolution that can be achieved for any delivered light in an AO system. Because retinal images as well as stimuli are built up as pixels defined by the scanned laser, the images do not actually represent the light intensity profile of the beam landing on the retina. In confocal systems, out of focus light is discarded in image reconstruction, yet such light remains present in the stimulus itself. To get a better idea of the true geometry for micron-scale stimuli, the point-spread function (PSF) of the optical system needs to be taken into account. For a typical field size used in our psychophysical experiments (~1.2° square), the sampling resolution is high enough for each photoreceptor to be imaged within about 10 pixels (Fig. 4.11a, b). A stimulus smaller than this, defined in image pixels, can theoretically be placed within the visible margins of a single cone.

One can estimate the actual stimulus shape by convolving the stimulus defined in pixels with the PSF. With AO correction, the incident beam aperture (5.6 mm in the example figure) yields a PSF with full width at half maximum of 24 arcsec, calculated with a 543 nm stimulus wavelength. Expressed in image space, this corresponds to a diameter of 2.6 pixels, or about 1.9 μm on the retina. Thus, with optimal wavefront correction, a nominal 3 × 3 pixel stimulus convolved with the PSF will produce a light intensity profile where the 5% intensity contour corresponds to an approximately circular area 7.3 pixels across (~5.3 μm on the retina), roughly matching the diameter of imaged cone apertures at 3.1° eccentricity (Fig. 4.11c). If we integrate the light falling within this 5% intensity contour, it represents ~80% of all light in the stimulus. Because cones vary in diameter with distance from the foveal center, stimuli can be scaled accordingly to match the cone diameters, if the appropriate PSF is used. This is the first of two steps used in characterizing the delivered microstimulus.

With any psychophysical testing, repeated stimulation under controllable conditions is necessary. Consequently, the second step in characterizing light delivery must take into account the spatial delivery errors that occur over each set of stimulus trials, after fixational eye movements had been compensated for with real-time eye tracking. Tracking the motion of the retina while a subject fixates involves reading the incoming video raster, comparing select portions of the raster to a reference frame, and then, as the raster approaches the site on the retina where stimuli are to

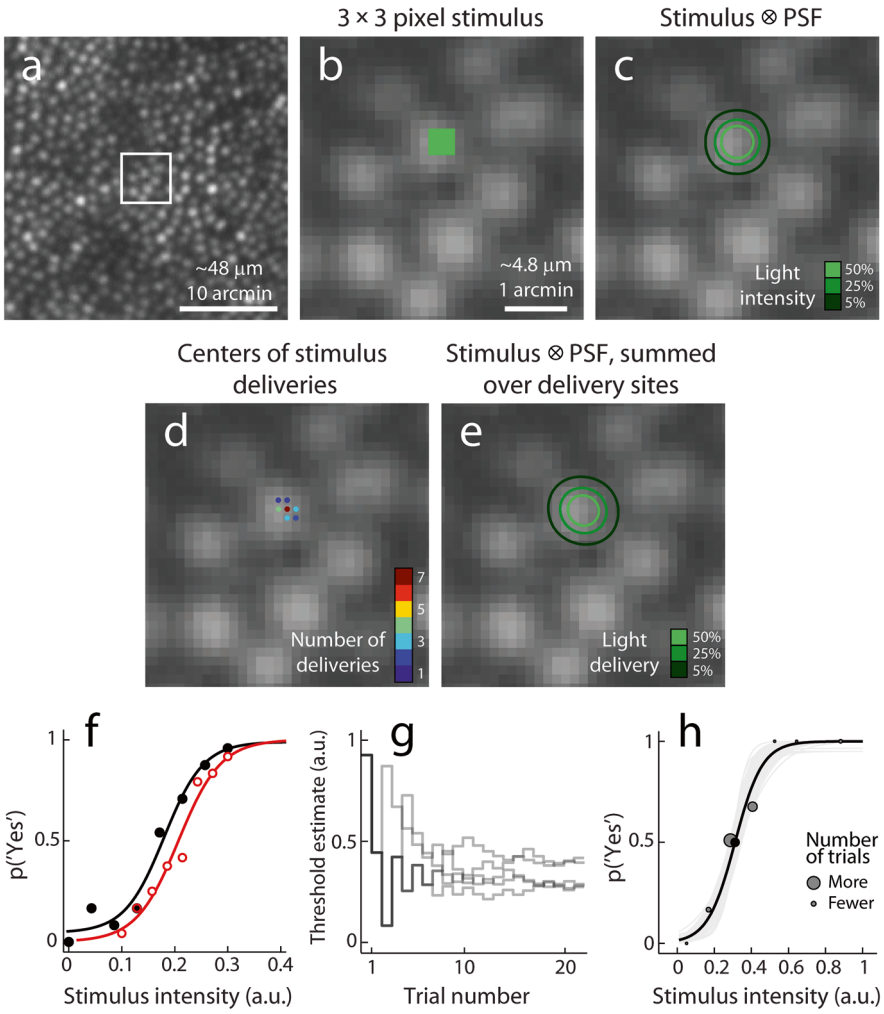

Fig. 4.11 Stimulus geometry, delivered light distribution, and psychometric results from cone-scale microstimulation. (**a**) AOSLO image of a human cone mosaic at 3.1° eccentricity, with outlined area scaled up in **b–e**. (**b**) Cone reflectance profiles at this eccentricity span ~7 pixels, nearly 5 µm in diameter. Microstimuli are specified in image pixels; here, a 3 × 3 pixel square. (**c**) Light intensity delivered to the retina is estimated by convolving the stimulus geometry with the diffraction-limited point-spread function of the eye. Intensity contours show that the light spreads over a broader area than the 3 × 3 specification. (**d**) Plot of actual delivery locations of the stimulus center relative to the targeted cone for a 22-trial psychophysical run. Positional delivery errors in eye motion correction causes stimulus deliveries to be jittered from trial to trial. (**e**) Cumulative distribution of light delivery on the retina during the run in **d**, derived from the diffraction-limited stimulus integrated over the actual delivery locations. (**f**) Psychometric frequency-of-seeing data and logarithmic fits from 2 subjects for the 3 × 3 pixel stimulus, obtained using a method-of-constant-stimuli approach ($n = 20$ trials per stimulus intensity). Because of daily instrument fluctuations in light levels, stimulus intensity is given in arbitrary units (a.u.). Eccentricity was 2.1° (black data) and 2.5° (red data). (**g**) Five runs of a staircase approach to measure luminance increment thresholds from one subject, illustrating some variability in the final threshold estimate (at last trial). (**h**) Staircase data in **g** converted into a frequency-of-seeing psychometric function (black line) based on boot-strapped fits (gray lines). (Panels **a–e** adapted from [167])

be delivered, predicting the movement of the eye just prior to stimulus delivery. Thus delivery accuracy depends, in part, on how far ahead in time the predicted location can be computed. Software operating at video frame rates in an AOSLO was developed to perform this eye tracking and stimulus delivery task [168]. In the current incarnation of this software, the prediction time can be as short as nearly 2 msec, yielding a standard deviation of 0.15 arcmin in the stimulus delivery positional error [169].

To illustrate how the eye tracking enables psychophysics based on microstimulation to be realized, Fig. 4.11d shows the delivery accuracy of repeated trials of a 3 × 3 pixel stimulus onto a targeted cone. The subject fixated a small luminous target superimposed into the visual field through a pellicle beam splitter. TCA offsets were measured using the method described previously. The center of one cone was selected in the infrared channel as the stimulus location, and TCA offsets were used to compensate for the lateral displacement of the green light stimulus relative to the infrared cone image. In the movie recorded during each trial, a fiducial cross is written into the frame at the location of the delivered stimulus. From this, we can recover each stimulus delivery location. In the given example, 7 out of 22 deliveries landed exactly at the targeted image pixel, with the remaining 15 deliveries distributed over the immediately neighboring pixels. From a series of similar experiments, the average standard deviation of delivery jitter was 2.2 pixels (in both x and y image coordinates), representing about 1.6 μm on the retina [167]. To make the final calculation of the light delivery profile, we sum the PSF-convolved nominal stimulus across the actual delivery locations (Fig. 4.11e), yielding the best estimate possible of the light distribution during one experiment. Integrating the light distribution within the 5% intensity contour shows that 82% of all the delivered light fell within this contour. Although this suggests that, even after repeated presentations, most of the delivered light was confined to a retinal area the size of a single cone, we note that this does not take into account uncontrollable light scatter (see below).

Under these conditions, we have found that robust psychophysical threshold functions can be measured for such cone-sized stimuli, whether using a classic method-of-constant-stimuli (Fig. 4.11f) or a Bayesian staircase approach (Fig. 4.11g, h). Out to about 5° eccentricity, subjects can be tested while targeting single cones. Beyond that eccentricity, we have found that more than one cone needs to be stimulated, at least for a luminance increment threshold task operating within the range of light intensity we can deliver [167]. This increase in threshold with eccentricity is consistent with prior studies using a constantly sized stimulus [170, 171]. Summation of input over multiple cones is likely to be required beyond 5° for stimuli to be effective at the perceptual level [172–174].

Further evidence that microstimuli can be utilized to probe single cones comes from the observation that thresholds are about 50% higher when stimuli land between cones, a finding that is largely explained by a linear model of the geometry of cone light capture [167]. The Gaussian profile of a cone's light capturing ability predicts that capture efficiency will be maximal at the cone's center and decline with increasing distance from the center. Such a prediction has been validated empirically at the level of the retina [98], at the main neural target of retinal projections, the lateral geniculate nucleus [129], and now at the perceptual level. The

visual system is thus exquisitely sensitive to the exact position of delivered stimuli, down to the micron scale. Characterizing microstimuli as we have, and with robust psychometric measurements now feasible, we are nearly poised to address how color percepts originate from the activity of single cones.

4.4.5 Psychophysical Testing and Variability

The evidence from the previous section suggests that the delivery accuracy for cone-sized stimuli can be good enough to resolve the spatial grain of the photoreceptor mosaic. Given the difficulty of directing stimuli to exactly the same location on a cone repeatably in the living eye, it is clear that a major source of variability in any perceptual task will be caused by stimulus delivery errors. Is any other source of psychophysical variability even detectable given the large effect of positional variability?

One way to address this issue is to test the same group of cones over multiple days. By measuring luminance increment thresholds for each cone using interleaved trials, one can control for factors such as daily variation in subject performance and in instrument light levels. Threshold values can be normalized against the mean threshold of the group to see how much variation occurs simply with repeated measurements, whether thresholds are consistent from day to day, and, perhaps most interestingly, whether cones exhibit different intrinsic thresholds. Figure 4.12 illustrates a few cone triplets that were studied this way, using the staircase method [175]. In Fig. 4.12a we measured thresholds multiple times on 3 separate days for one triplet and found no difference in threshold among any of the cones. It is evident that repeated measurements of thresholds are inherently noisy, as they can vary by as much as 60% from one measurement to the next. Some of this variation must be noise associated with doing psychophysical threshold tasks, and some is undoubtedly due to positional delivery error (an error that includes transient TCA shifts that cannot be measured during the course of the experiment). An examination of threshold versus delivery location revealed that about 50% of the variance in the measured thresholds come from experimental errors, if it is assumed that cone thresholds are identical [80, 167].

Physiological data, however, have shown that cone thresholds may not all be the same. As we noted earlier, when the functional weighting of cones were measured in macaque retina, it was found that each retinal ganglion cell was receiving input from a handful of cones expressing a range of synaptic weights [98, 99]. Such a result raises the question of whether differential cone weighting in the retina could be propagated to the perceptual level. Figure 4.12b provides evidence that such functional weighting can be measured psychophysically. Here, a triplet of cones was measured repeatedly over several days, with one cone having a significantly higher threshold than the other two. The high-threshold cone needed about 40% more light in the stimulus in order to be detected. Although there is no way to determine if all the cones in this triplet are connected to the same retinal ganglion cell, this result suggests that differential functional weighting—either from cones to

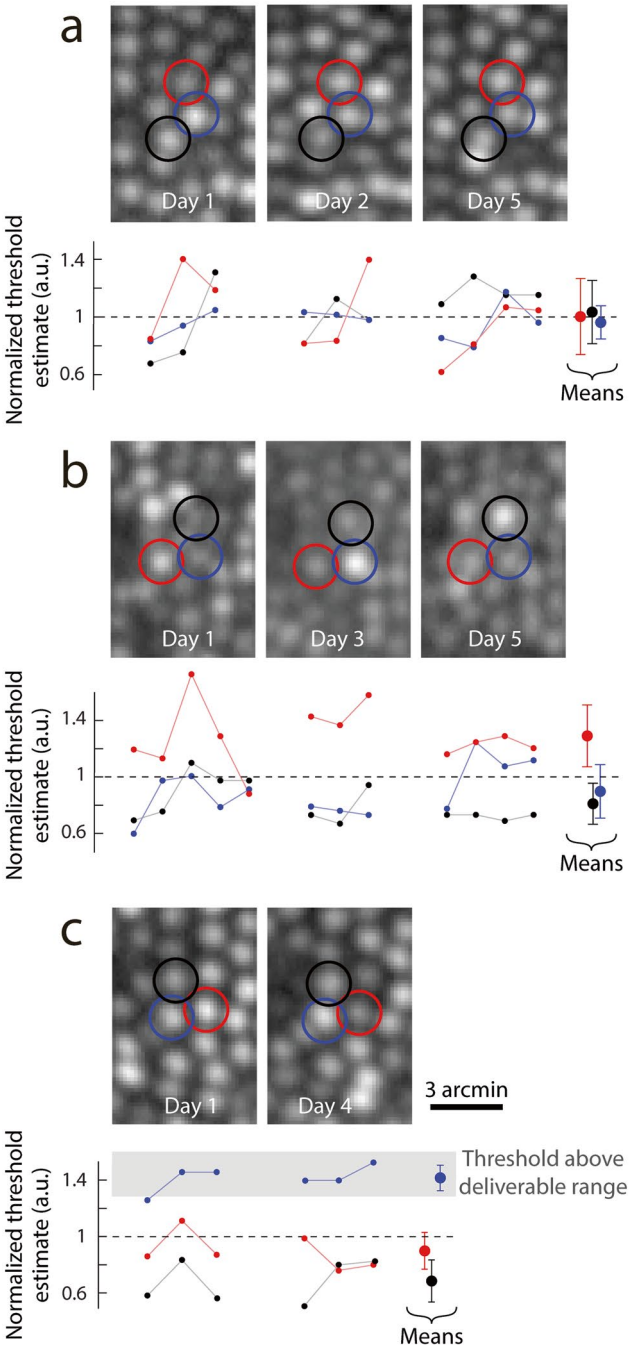

Fig. 4.12 Luminance increment thresholds measured with microstimulation are associated with specific cones. The AOSLO images show the human cone triplets studied over multiple days in different subjects. Cones targeted for stimulation and the thresholds from each are coded by color.

ganglion cells or between two ganglion cells—can be detected perceptually. Near neighbor cones can vary in their threshold sensitivity by as much as 80% when tested during the same experiment [175]. The important point is to realize that no two L or M cones can be assumed to have the same luminance increment threshold.

Additional evidence that microstimulation can generate cone-specific responses comes from the occasional encounter with a candidate S cone. The stimulus wavelength band used during the two previous examples was 543 ± 11 nm, a range that is absorbed equally well by L and M cone opsins. For an S cone to produce an equivalent response with this wavelength, it would need ~400 times more light than an L or M cone [41]. This amount of light exceeds the range our current AOSLO can deliver. So, under these experimental conditions, if an S cone was probed, the subject would respond "not seen" during most trials and drive the staircase above the deliverable range. One of the cones in the triplet illustrated in Fig. 4.12c had just such an outcome. Given that the other two cones had reliable thresholds measured across 2 days, this result suggests that the cone with unmeasurable threshold was an S type. Additional data given in the next section confirms that such psychophysical outcomes can be associated with S cones.

Although prone to a high degree of variability, most likely caused by positional errors in stimulus delivery, reproducible perceptual data can be acquired with cone-targeted microstimulation. The fact that relative increment thresholds between neighboring cones are consistent from day to day, and that they can be consistently distinct, implies that the perceptual discriminations are essentially driven by signals arising from individual cones.

4.5 Psychophysical Cone Classification

Having discussed the main experimental constraints that need to be faced when trying to extract perceptual data from microstimulation, we now review a number of previous studies, as well as some work in progress, that have revealed cone-specific responses in the human retina. Although considerable insights have been made in relating inferred cone mosaics to color phenomenon without the use of AO-based imaging (e.g. [72, 176, 177]), we will be focusing here on work that has relied on imaged cone mosaics to strategically test for cone-driven percepts.

Fig. 4.12 (continued) Data are grouped by test day and were normalized to the mean threshold of the triplet (to control for small day-to-day changes in stimulus light levels). Each cone was tested 3–5 times per experiment (small dots), using 543 ± 11 nm light, a wavelength equally absorbed by L and M cones. Mean single-cone thresholds (±1 SD) across all days are shown on the right within each graph. In (**a**) all cones had similar increment thresholds, while in (**b**) the cone circled in red had consistently higher thresholds than the other two cones in its triplet. In (**c**) the cone circled in blue had thresholds beyond the range of deliverable light (indicated by shading), which suggests it is an S cone, given the stimulus conditions. (Adapted from [175])

4.5.1 S Cone Testing

Once it was appreciated that S cones are relatively uncommon yet regularly spaced members of the cone mosaic, it was realized that it may be possible to map them out psychophysically by probing with small S-cone-isolating stimuli. Williams et al. (1981) set out to do just that. Presenting a 1.1 arcmin spot of 420 nm light for 50 msec over a grid of locations at and around the fovea, they measured thresholds in the presence of a background light that adapted out L and M cone responses [178]. Sensitivity for these stimuli was relatively low at the center of fixation, and increased by about 1 log unit within 15 arcmin of the fovea. Control experiments showed that this sensitivity profile was not due to light absorption by the macular pigment lying in front of the photoreceptors. Such perceptual data is consistent with the known absence of S cones in the foveola [48, 49]. More tellingly, the sensitivity terrain around the fovea contained peaks and valleys with about the same spacing as that subsequently observed histologically for S cones. Repeat measurements over a 2 year timespan suggested that the retinal location of these S cone sensitivities were stable. A model of light capture under their experimental conditions, assuming single S cones were the detectors, was also consistent with the psychometric data produced by varying stimulus intensities. Taken together, the most parsimonious explanation of their results was that S cones could indeed be mapped, though in small numbers. Such experiments are taxing, as the authors noted, and having to probe randomly across a coarse grid, the chances of stimuli landing directly on a cone are low. Nonetheless, this early study held promise that single cone activity could be detected perceptually and helped to encourage the development of techniques for imaging cones and enable cone-targeted stimulation.

4.5.2 Dysfunctional and Dysflective Cone Testing

After AO-corrected retinal imaging became available, finer spatial testing of perception could be achieved because the stimuli impinging on the retina were no longer blurred by optical aberrations. In a situation somewhat converse to the S cone mapping, sensitivity losses might be expected in cone mosaics with lacunae—if stimuli were truly small enough. To learn if such microscotomas could be detected, a retina was studied in a deuteranopic subject that had dysfunctional cones due to a mutant M photopigment [179]. In AO images from this subject, about 30% of the cones appeared relatively dark compared to most cones, suggesting that the mutation either damaged the cones or lead to outright cone loss. Cone-sized stimuli of 550 nm were flashed for 46 msec at various locations all 0.5° from a fixation spot, in an effort to see if a suitable proportion of these AO-corrected stimuli would not be perceived. Comparison of the deuteranope's frequency-of-seeing curves to those of control subjects showed that mutant cones did cause a lower sensitivity and slope in the curve, as predicted by a model of cone loss. Larger stimuli, such as those used

in clinical exams, showed no difference between the M-cone-compromised subject and controls. Microstimuli, therefore, appeared to unmask microscotomas. This was another piece of evidence telling us that perceptual effects can rest on the activity—or inactivity in this case—of single cones.

Unlike phenotypic losses in subjects with color vision deficiencies, it is wholly expected that retinal degeneration of various types would also lead to perceptual loss at the cone scale [180]. Several studies have reported just that [181–183]. Here, however, it is important to just emphasize the finding that cones can be fully functional but appear to be non-reflective in AOSLO imaging, a status called dysflective cones [182, 184]. They occur because of likely morphological anomalies that prevent light from being adequately sent back to the photodetector in AO systems, and they appear dark in normal as well as diseased retinas. Dysflective cones can be hypo-reflective for well over a year, and can also be quite transient [163, 185]. When directly tested with microstimulation, dysflective cones appear to have the same increment threshold sensitivity as their normally reflecting neighbors, affirming their unaltered function in the face of abnormal reflectivity [163]. Thus it should be recognized that the reflective status of a cone does not readily indicate its functional status, which means interpreting cone function based on reflectivity alone needs to be done with care.

4.5.3 Cone Spectral Identification and Match with Absorptance Imaging

In a previous section, we elaborated on the considerations that need to be made in developing techniques for single cone microstimulation. One of the obvious interests in these techniques is to learn if individual cones can be classified by spectral type psychophysically. Given the many stages of post-receptoral processing that intervene between cones and perception, it is not necessarily the case that activation of a single cone will lead to a veridical representation of that cone's spectral class. Retinal circuitry imposes an opponency signal between L and M cones that may variably dilute the signal from either of these cone types. Cortical circuitry—about which much less is known (see Chap. 8)—may also be altering the sensory input. To put such psychophysical experiments on firmer footing, therefore, a comparison with an objective method such as absorptance imaging seems sensible. Here we describe our efforts in comparing the biophysical and psychophysical mapping of the same set of cones.

An experiment was designed to optimize distinguishing L from M cones perceptually. With a sensitivity difference between these two cones of ~0.05 log units at their peak wavelengths [41], it was unlikely that comparing responses between stimuli of 561 and 531 nm would yield reliable classification given the variability of measuring thresholds with microstimulation [74] (Fig. 4.12). Instead, the strategy was to isolate responses from L cones alone, with M cones identified separately.

First, we used a 710 nm spot stimulus for measuring increment thresholds, as this wavelength represents the maximum sensitivity difference between L and M cones. Second, we presented the microstimuli against a constant L-cone-isolating background of 470 nm light [186]. Taking the remaining light in the imaging field into account (Fig. 4.13a), these stimulus conditions are predicted to have an L:M sensitivity ratio of about 24:1, and S cones would be unresponsive [187]. Thus, over the range of deliverable light intensity (scaled 0 to 1 in arbitrary units), if the average L cone had a threshold above 0.05, then any M or S cones encountered would register thresholds greater than 1. To avoid issues concerning subject fatigue that might alter threshold, 2 or 3 cones were tested simultaneously by randomly interleaving trials, with independent staircases running on each selected cone. When cones with off-scale thresholds were encountered, the adapting background light was then switched off and the threshold re-measured. If the sensitivity recovered, such cones were classified as M type (Fig. 4.13b, c). A similar approach using M-cone-isolating conditions was used on the same cones to identify M cones perceptually (Fig. 4.13d–f).

Increment thresholds measured under cone-isolating conditions for a group of cones mapped over several days showed wide bimodal distributions. The broad range of L and M cone thresholds (Fig. 4.13g, h) arises from several factors. Two we have already highlighted in this chapter: intrinsic variability of threshold among cones, and positional noise in stimulus delivery. A third factor is a contribution from cones surrounding the one targeted for stimulation. L and M cones are electrically coupled via gap junctions [188, 189]. A Monte Carlo simulation of the effect of varying the composition of the surrounding cones suggests that ~20% of the threshold range could be due to adaptation state differences in those surrounding cones [74, 190]. One can appreciate the possible impact of surrounding cones in a map where each cone is color-coded by its mean threshold value, as there are a number of instances where a gentle gradation of threshold differences exists between cones (Fig. 4.13g, h). On the whole, however, such a map is more remarkable for the many cases where neighboring cones have sizable threshold differences—often shifting from a value 0.5 to "unseen" from one cone to the next.

To confirm that microstimulation can classify cones psychophysically, the same set of cones in this subject was also classified using absorptance imaging. The method used here was modified because a scanning AO system was used rather than

Fig. 4.13 (continued) errors in delivery. (**c**) Example threshold data for Cones 1 and 2. With the adapting field on, Cone 1 was sensitive to the stimulus, making it a likely L cone, but Cone 2 was not unless the adapting light was off (control), making it a candidate M cone. (**d–f**) Data for M cone isolating tests of the same cones as in **b**. (**g, h**) Threshold maps for a set of cones in one subject, with Cones 1 and 2 indicated. (**i**) Pseudocolor image of the same cone mosaic as shown in **g, h**, but derived from AOSLO imaging and retinal densitometry. Red, green, and blue labels correspond to L, M, and S cones, respectively. (**j**) Histograms of cone thresholds collected against M-or L-cone adapting backgrounds for 2 subjects. Densitometric identities are plotted up for L cones and down for M/S cones. A classification criterion (gray dashed line) delineated cones belonging to the classes differentiated by the perceptual task, with filled color bars being cones behaving according to their spectral type. (Adapted from [74])

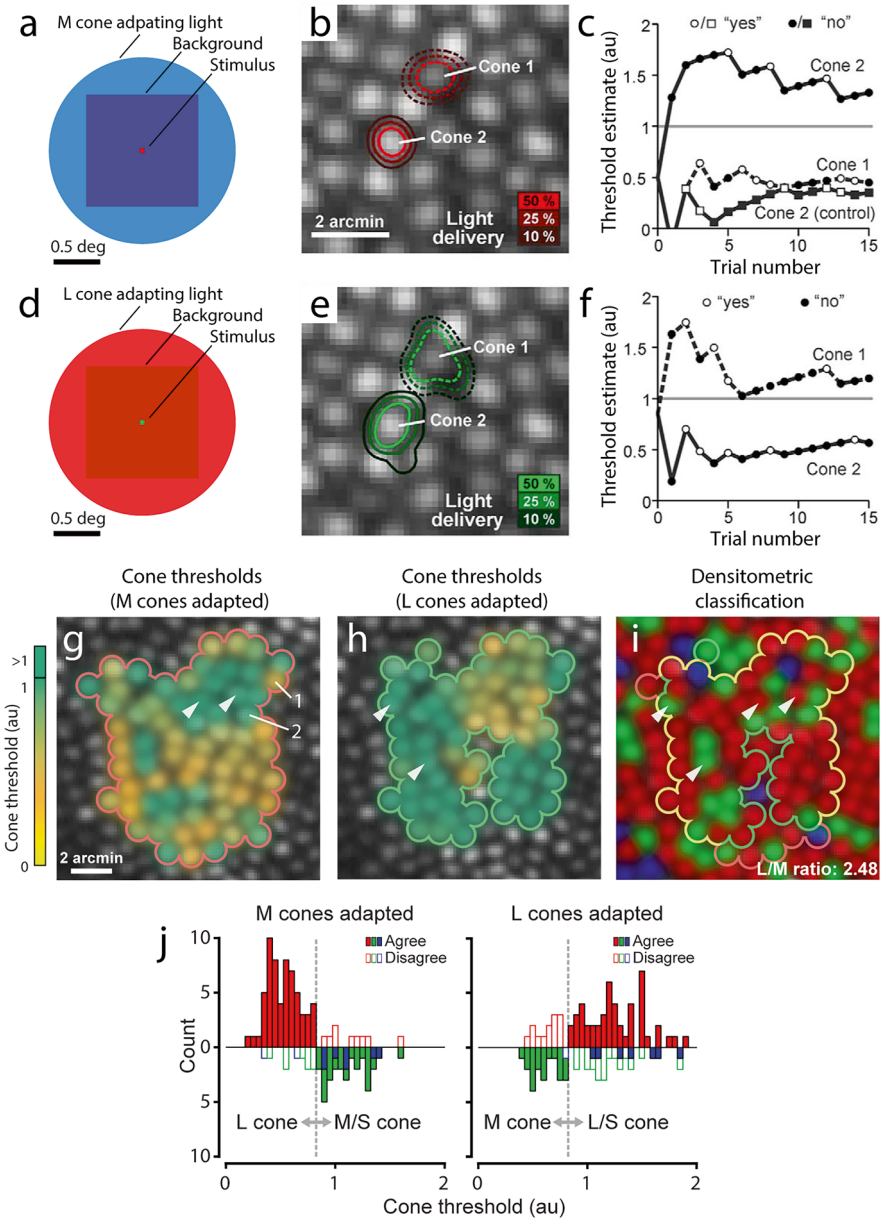

Fig. 4.13 Functional cone classification in the living eye. (**a**) Schematic of L cone isolating conditions as seen by a subject. A 2° adapting light (peak wavelength = 470 nm) is used to counterbalance light adaptation caused by instrument light leak in the imaging field. This blue light adapts M and S cones preferentially, leaving L cones >20 times more sensitive to a 710 nm test flash (small red square). (**b**) Stimulus light delivery distribution for two targeted cones plotted on the AOSLO image. The contour lines (Cone 1 = dashed; Cone 2 = solid) indicate the stimulus light intensity accumulated over 15-trial staircases, incorporating a diffraction blur of the 3 × 3 pixel stimulus and

a flood AO system, but the underlying principles were the same. Dynamic differential cone bleaching was performed under two different conditions to distinguish S from L or M cones, and separately, L from M cones [44]. The resulting cone map revealed L and M cones in a 2.1:1 ratio (Fig. 4.13i). To make a comparison between the threshold maps and absorptance images, the former's thresholds need to be converted into a true 3-cone classification. This was done using Cohen's kappa coefficient, a statistic of agreement for categorized data [191]. Across 2 subjects, a threshold criterion (dashed line in Fig. 4.13j) yielded the best agreement between the two maps for L and M cones. The four S cones in the example field, which are more reliably identified by differential bleaching [43, 69, 192], all had thresholds exceeding 1, as expected for these stimuli. For all of the L and M cones across the subjects, there was 77% agreement between the two methods—a reasonably good match between subjective and objective methods of cone classification. Under these stimulus conditions, at least near the fovea, signals from individual cones do indeed seem to propagate from the retina to the perceptual level, carrying their spectral identity with them. Such data effectively redefine the groundwork for experiments asking elementary questions about the cellular basis of color percepts, a topic we touch on next.

4.5.4 Color Appearance of Microstimuli

Early efforts at using small stimuli and standard optical correction to probe color appearance revealed that subjects often required a range of hue options to categorize monochromatic lights (reviewed in [88]). A genuine impediment for an adequate interpretation of these results is that the underlying cone mosaics were not known, for both the relative numbers and the spatial arrangement of the cones are likely to produce different color signals depending on where the stimuli land from trial to trial. In addition, uncorrected optical blur will broaden any stimuli, and particularly at the fovea this would activate many more than one cone. Both of these hurdles were removed in a study that used AO correction along with classified cone mosaics to see how color sensations were generated [78]. Briefly flashed microstimuli of ~0.3 arcmin were presented in a retinal locus near 1° where the cones had been mapped by absorptance imaging. The stimuli varied in two important ways: by wavelength (500, 550, or 600 nm) and by position (5 sites within a 14 arcmin square, with fixational eye movements uncompensated). These parameters allowed the authors to distinguish between the influence of wavelength versus cone composition on color appearance. All subjects required white plus up to 7 hues to categorize their percepts. The range of hues was generally independent of stimulus wavelength, but did depend on L:M cone ratio. When the ratio was weighted toward M cones, more greenish hues and fewer reddish hues were needed to describe the colors, and vice-versa in subjects with more L cones. Blue and purple categories were also required, which the authors suggest may arise through strongly activated M cones mimicking the L:M excitation ratio of bluish light.

Because this result implies that different color sensations originate from the stimulation of one cone, the role of the surrounding cones naturally comes into question. If one cone was stimulated within a small field of identical cones, the L/M opponent mechanism may not be driven and a "white" response would be predicted (and was indeed frequently reported). A statistical approach was pursued to see if this and the other reported hues could be explained by a stimulated cone surrounded by different proportions of other cone types [84]. The resulting model broadly captured the color-naming data from Hofer et al. (2005) and is consistent with the idea that the contributions of individual cones to color percepts is dependent to some degree on the local arrangement of cones. However, the psychophysical data could never be predicted exactly because the precise location of the stimulus on a trial-by-trial basis was not known.

To correlate each trial's response with the cone being tested requires cone-targeted microstimulation, like what we have already described. Comprehensive data from such an experiment has also revealed a family of color appearances [193], even when the same cone was stimulated repeatedly with 543 nm light on a neutral white background (Fig. 4.14). Veridical percepts would appear green in this paradigm only if the stimulus wavelength was mediating the color sensation. In the results shown here, the subject reported only red, green, white, and "not seen" among the available response categories, which included blue and yellow. Notably, in trials when a color other than white was reported, L cones most frequently lead to red responses, and M cones to reports of green, with a high consistency in these reports. White responses were more common than in the subject with a similar L:M cone ratio in Hofer et al. 2005, but this may have been due to differences in the stimulus background (Hofer et al. 2005 used dark background while Sabesan et al. 2016 used a brighter neutral gray background). From 2 subjects tested with this approach, it appeared that when all the surrounding cones were of opposite type, subjects were not more likely to perceive a color rather than white, suggesting that midget retinal ganglion cells may not have played a prominent role in this task. Several of the cones were tested again on separate days and often yielded the same responses. The main indications from this work is that color appearance is testable at the cellular scale and depends on the cone being stimulated. Because the underlying cell types that are processing these signals remain unknown for this task (e.g., midget or parasol retinal ganglion cells?), a more comprehensive picture of how color percepts emerge from the retina still awaits further work.

Technical improvements have now enabled tracking and targeting of multiple cones. Color sensations elicited by targeting and stimulating proximal pairs of cones of known type yield an appearance that is largely explained by linear summation, but with a systematic amplification of saturation whenever two cones of like-type were stimulated [194]. While studies involving single cones or cone pairs can be very informative about basic mechanisms of color perception, many aspects of color appearance are better studied when delivered over larger fields. To that end, cone targeted stimulation has progressed to the point where all cones within an AOSLO field can be tracked and targeted with light. The stimulus platform is called Oz and broadens the scope of color science that can be done [195]. Within the Oz platform,

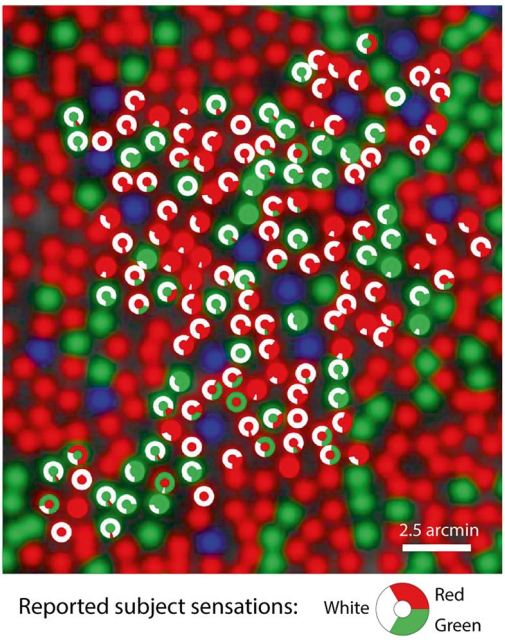

Fig. 4.14 Comparison of cone type and color naming responses. A field of human cones classified by AOSLO absorptance imaging (as described in Fig. 4.13) was tested for color categorization with 0.5 sec retinally-stabilized flashes of 543 nm cone-sized microstimuli, in the presence of a neutral white background. The subject was allowed to respond in one of 5 ways (white, red, green, blue, yellow), and the proportion of the responses for detected stimuli are illustrated in the circular histograms surrounding each tested cone (20 trials apiece). The data shown are compiled from multiple sessions where several cones were stimulated with interleaved trials. In most instances, stimulation of L cones led to red or white responses, while green or white was reported when M cones were stimulated. Blue or yellow percepts were never reported. Eccentricity = 1.5°. (Adapted from [192])

an AOSLO becomes a display that can control the activation level of each individual cone within the field on each frame, bypassing limits imposed by optical blur, eye movements and even the spectral sensitivities of the cones themselves. The first experiments using this platform tested color sensations elicited by targeting thousands of cones of like type within an AOSLO field. As anticipated, this stimulus elicited a broad range of color sensations. For example, when targeting only L cones over a 1° × 1° square patch with green 543 nm light, subjects reported a reddish-orange color appearance. When only M cones were stimulated, subjects reported a deeply saturated blue-green color. Formal color matching revealed that the color appearance elicited by M-only stimulation was outside of the normal human color gamut (Fig. 4.15). How might this occur? The reasoning is this: the spectral sensitivities of S, M, and L cones overlap, so there is no natural light that can stimulate M cones only. Therefore, an unprecedented signal reaches the brain when only M cones are stimulated, which the eye perceives as being ultra-saturated. This result

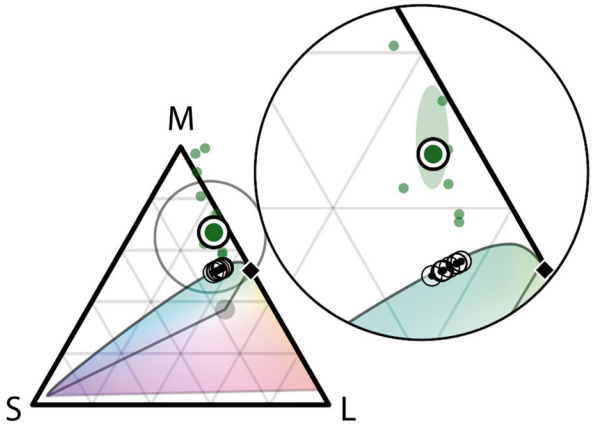

Fig. 4.15 Color appearance data plotted on a Maxwell triangle with barycentric coordinates. The colored region indicates the typical human color gamut, whose extent in the M-direction is limited by the spectral sensitivity overlap of M cones with L and S cones. The black diamond indicates the color of the 543 nm laser light source used to stimulate the cones. The green dots indicate the out-of-gamut individual color appearances (small dots) and average (large dot) respectively when M cones are stimulated with the Oz platform. The green shaded region indicates the uncertainty ellipse for the average color estimate (3 times the just noticeable difference estimate). (Adapted from [194])

may be thought of as the perception of a new color: one that could be quantified, although not readily appreciated. The development of a unique and stable percept to a novel sensory input might take time or might never happen, as with other sensory modalities, so more research needs to be done. The Oz platform is not only capable of expanding the gamut of trichromatic color vision but could be used, in principle, to expand the dimensionality of color vision by stimulating one or more separate subsets of cones as though they had different spectral sensitivities than L, M or S photopigments under natural conditions.

4.6 Conclusions and Caveats

The central points of this chapter bear on how the cone mosaic in trichromatic primates can be fruitfully explored, and what factors might guide the interpretation of experimental results. Here we summarize those points:

- Light absorption by photopigments (densitometry) can be used to objectively map cone arrays in a variety of imaging modalities.
- Cone composition varies widely from subject to subject, and regionally within a single retina; random arrangement cannot be assumed.
- The functional weighting of each cone is not a constant; at both the ganglion cell and perceptual levels, the strength of each cone's input varies.

- Cellular-scale testing in vivo requires compensation of the eye's optics, motion, and vasculature for the most uncompromised delivery of microstimuli.
- Color percepts that ensue from cone-sized stimuli appear to be most influenced by signals from individual cones.
- Cone classification maps in the very center of the fovea have yet to be made (due to optical limitations with small cones), so cone-resolved color sensations from here remain untapped.

Given the psychophysical results described in this chapter, it may be tempting to think that "single-cone psychophysics" has been realized. We have avoided the phrase, for it carries the implication that a percept is being determined by light absorption in only one cone, and nothing more. There is no direct evidence that only one cone is being activated by microstimuli, and it seems unlikely this can ever be garnered from in vivo studies. In fact, by optical diffraction alone, the delivered light profile cannot be restricted to one cone. The point-spread function, calculated from a model eye, includes a first Airy ring with an amplitude of ~1% of the central peak. From the light intensity profile shown in Fig. 4.7c, this would mean that the immediately neighboring cones situated around a cone targeted for stimulation would have a chance to absorb a few percent of the total light. Intraocular scatter occurring along the light path in front of the retina would divert an additional small fraction of light onto these surrounding cones (reviewed in [196]). Together with the point-spread function, a more realistic light distribution profile might have ~20% of all the light falling outside the diameter of the inner segment of a targeted cone, a factor that will depend on cone size and pupil size in AO systems [197]. It is important to realize, however, that this skirt of light is distributed over a very broad area and would activate most cones weakly. Some of this activity may be modulating percepts to varying degrees, depending on stimulus conditions, as we have seen.

The light profile itself is not the only factor that affects percepts resulting from a micron-scaled stimulus. Inner retinal wiring, ongoing levels of activity in the cones, varying functional weighting from cones to ganglion cells, and which ganglion cell type is actually propagating the signal to cortex for a particular stimulus condition—these all come into play and are the objects of future research. Functional maps of the cone mosaic will ultimately come in different flavors, given each cone's divergent input to many cell types as well as the stimulus conditions being faced. For psychophysicists, AO-corrected microstimulation may become a useful tool for making such maps, because it simply allows researchers to pour more light into any one cone of interest. Like drops hitting an ocean, they make ripples we can occasionally see—were it the visual system, the drops would sometimes have a color of their own.

Acknowledgements We thank J. K. Bowmaker, K. S. Bruce, E. J. Chichilnisky, G. D. Field, J. D. Mollon, R. F. Cooper, J. I. W. Morgan, and B. Schmidt for generously providing materials for figures. For improving the text, we are grateful to K. S. Bruce, T. W. Kraft, M. S. Loop, and A. S. McKeown. Our work has been supported by the National Eye Institute (L.C.S., W.S.T., A.R., R.S.), the Air Force Office of Scientific Research (A.R., R.S., L.C.S.), the Eyesight Foundation of Alabama (L.C.S.), Fight for Sight (R.S.), the American Optometric Foundation (W.S.T.), the German Research Council (W.M.H.), and a Career Award at the Scientific Interfaces from the Burroughs Wellcome Fund (R.S.).

References

1. Thoen HH, How MJ, Chiou TH, Marshall J. A different form of color vision in mantis shrimp. Science. 2014;343(6169):411–3.
2. Curcio CA, Sloan KR, Kalina RE, Hendrickson AE. Human photoreceptor topography. J Comp Neurol. 1990;292(4):497–523.
3. Cooper RF, Kalaparambath S, Aguirre GK, Morgan JIW. Morphology of the normative human cone photoreceptor mosaic and a publicly available adaptive optics montage repository. Sci Rep. 2024;14(1):23166.
4. Williams DR. Imaging single cells in the living retina. Vis Res. 2011;51(13):1379–96.
5. Roorda A. Adaptive optics for studying visual function: a comprehensive review. J Vis. 2011;11(7)
6. Berendschot TT, DeLint PJ, van Norren D. Fundus reflectance--historical and present ideas. Prog Retin Eye Res. 2003;22(2):171–200.
7. Rodieck RW. The first steps in seeing. Sunderland: Sinauer; 1998.
8. Packer OS, Williams DR, Bensinger DG. Photopigment transmittance imaging of the primate photoreceptor mosaic. J Neurosci. 1996;16(7):2251–60.
9. Enoch JM, Tobey FL. Vertebrate photoreceptor optics. Berlin: Springer-Verlag; 1981.
10. Marcos S, Burns SA. Cone spacing and waveguide properties from cone directionality measurements. J Opt Soc Am A Opt Image Sci Vis. 1999;16(5):995–1004.
11. Vohnsen B, Iglesias I, Artal P. Guided light and diffraction model of human-eye photoreceptors. J Opt Soc Am A Opt Image Sci Vis. 2005;22(11):2318–28.
12. Lakshminarayanan V, Enoch JM. Biological waveguides. In: Bass M, Enoch JM, Lakshminarayanan V, editors. Handbook of optics. New York: McGraw-Hill; 2010.
13. Vohnsen B. Directional sensitivity of the retina: a layered scattering model of outer-segment photoreceptor pigments. Biomed Opt Express. 2014;5(5):1569–87.
14. Stiles CW, Crawford BH. The luminous efficiency of rays entering the eye pupil at different points. Proc R Soc Lond B Biol Sci. 1933;112:428–50.
15. Applegate RA, Lakshminarayanan V. Parametric representation of Stiles-Crawford functions: normal variation of peak location and directionality. J Opt Soc Am A. 1993;10(7):1611–23.
16. Chen B, Makous W. Light capture by human cones. J Physiol. 1989;414:89–109.
17. MacLeod DI, Williams DR, Makous W. A visual nonlinearity fed by single cones. Vis Res. 1992;32(2):347–63.
18. Chen B, Makous W, Williams DR. Serial spatial filters in vision. Vis Res. 1993;33(3):413–27.
19. Meadway A, Sincich LC. Light reflectivity and interference in cone photoreceptors. Biomed Opt Express. 2019;10(12):6531–54.
20. Gao W, Cense B, Zhang Y, Jonnal RS, Miller DT. Measuring retinal contributions to the optical Stiles-Crawford effect with optical coherence tomography. Opt Express. 2008;16(9):6486–501.
21. Jonnal RS, Besecker JR, Derby JC, Kocaoglu OP, Cense B, Gao W, Wang Q, Miller DT. Imaging outer segment renewal in living human cone photoreceptors. Opt Express. 2010;18(5):5257–70.
22. Jonnal RS, Kocaoglu OP, Zawadzki RJ, Lee SH, Werner JS, Miller DT. The cellular origins of the outer retinal bands in optical coherence tomography images. Invest Ophthalmol Vis Sci. 2014;55(12):7904–18.
23. Miller DT, Williams DR, Morris GM, Liang J. Images of cone photoreceptors in the living human eye. Vis Res. 1996;36(8):1067–79.
24. Wade A, Fitzke F. In vivo imaging of the human cone-photoreceptor mosaic using a confocal laser scanning ophthalmoscope. Lasers Light Ophthal. 1998;8(3):129–36.
25. Vohnsen B, Iglesias I, Artal P. Directional imaging of the retinal cone mosaic. Opt Lett. 2004;29(9):968–70.
26. Pircher M, Baumann B, Gotzinger E, Hitzenberger CK. Retinal cone mosaic imaged with transverse scanning optical coherence tomography. Opt Lett. 2006;31(12):1821–3.

27. Williams DR, Burns SA, Miller DT, Roorda A. Evolution of adaptive optics retinal imaging [invited]. Biomed Opt Express. 2023;14(3):1307–38.
28. Porter J, Queener H, Lin J, Thorn K, Awwal A. Adaptive optics for vision science. Hoboken: Wiley-Interscience; 2006.
29. Liang J, Williams DR, Miller DT. Supernormal vision and high-resolution retinal imaging through adaptive optics. J Opt Soc Am A Opt Image Sci Vis. 1997;14(11):2884–92.
30. Roorda A, Romero-Borja F, Donnelly WJ 3rd, Queener H, Hebert T, Campbell M. Adaptive optics scanning laser ophthalmoscopy. Opt Express. 2002;10(9):405–12.
31. Miller DT, Kurokawa K. Cellular-scale imaging of transparent retinal structures and processes using adaptive optics optical coherence tomography. Annu Rev Vis Sci. 2020;6:115–48.
32. Rushton WA. Pigments and signals in colour vision. J Physiol. 1972;220(3): 1P-P.
33. Marks WB, Dobelle WH, Macnichol EF Jr. Visual pigments of single primate cones. Science. 1964;143(3611):1181–3.
34. Baylor DA, Nunn BJ, Schnapf JL. Spectral sensitivity of cones of the monkey Macaca fascicularis. J Physiol. 1987;390:145–60.
35. Schnapf JL, Kraft TW, Nunn BJ, Baylor DA. Spectral sensitivity of primate photoreceptors. Vis Neurosci. 1988;1(3):255–61.
36. Schnapf JL, Kraft TW, Baylor DA. Spectral sensitivity of human cone photoreceptors. Nature. 1987;325(6103):439–41.
37. Dartnall HJ, Bowmaker JK, Mollon JD. Human visual pigments: microspectrophotometric results from the eyes of seven persons. Proc R Soc Lond B Biol Sci. 1983;220(1218):115–30.
38. Stockman A, Sharpe LT, Merbs S, Nathans J. Spectral sensitivities of human cone visual pigments determined in vivo and in vitro. Methods Enzymol. 2000;316:626–50.
39. Bowmaker JK, Dartnall HJ. Visual pigments of rods and cones in a human retina. J Physiol. 1980;298:501–11.
40. Nork TM, McCormick SA, Chao GM, Odom JV. Distribution of carbonic anhydrase among human photoreceptors. Invest Ophthalmol Vis Sci. 1990;31(8):1451–8.
41. Stockman A, Sharpe LT. The spectral sensitivities of the middle- and long-wavelength-sensitive cones derived from measurements in observers of known genotype. Vis Res. 2000;40(13):1711–37.
42. Mollon JD, Bowmaker JK. The spatial arrangement of cones in the primate fovea. Nature. 1992;360(6405):677–9.
43. Roorda A, Williams DR. The arrangement of the three cone classes in the living human eye. Nature. 1999;397(6719):520–2.
44. Sabesan R, Hofer H, Roorda A. Characterizing the human cone photoreceptor mosaic via dynamic photopigment densitometry. PLoS One. 2015;10(12):e0144891.
45. Bowmaker JK, Dartnall HJ, Mollon JD. Microspectrophotometric demonstration of four classes of photoreceptor in an old world primate, Macaca fascicularis. J Physiol. 1980;298:131–43.
46. Marc RE, Sperling HG. Chromatic organization of primate cones. Science. 1977;196(4288):454–6.
47. de Monasterio FM, McCrane EP, Newlander JK, Schein SJ. Density profile of blue-sensitive cones along the horizontal meridian of macaque retina. Invest Ophthalmol Vis Sci. 1985;26(3):289–302.
48. Wikler KC, Rakic P. Distribution of photoreceptor subtypes in the retina of diurnal and nocturnal primates. J Neurosci. 1990;10(10):3390–401.
49. Curcio CA, Allen KA, Sloan KR, Lerea CL, Hurley JB, Klock IB, Milam AH. Distribution and morphology of human cone photoreceptors stained with anti-blue opsin. J Comp Neurol. 1991;312(4):610–24.
50. Lennie P, Movshon JA. Coding of color and form in the geniculostriate visual pathway. J Opt Soc Am A Opt Image Sci Vis. 2005;22(10):2013–33.
51. Kolb H, Dekorver L. Midget ganglion cells of the parafovea of the human retina: a study by electron microscopy and serial section reconstructions. J Comp Neurol. 1991;303(4):617–36.

52. Dacey DM. The mosaic of midget ganglion cells in the human retina. J Neurosci. 1993;13(12):5334–55.
53. Wassle H, Grunert U, Martin PR, Boycott BB. Immunocytochemical characterization and spatial distribution of midget bipolar cells in the macaque monkey retina. Vis Res. 1994;34(5):561–79.
54. Wassle H, Grunert U, Rohrenbeck J, Boycott BB. Cortical magnification factor and the ganglion cell density of the primate retina. Nature. 1989;341(6243):643–6.
55. Calkins DJ, Sterling P. Absence of spectrally specific lateral inputs to midget ganglion cells in primate retina. Nature. 1996;381(6583):613–5.
56. Dacey DM, Lee BB, Stafford DK, Pokorny J, Smith VC. Horizontal cells of the primate retina: cone specificity without spectral opponency. Science. 1996;271(5249):656–9.
57. Jusuf PR, Martin PR, Grunert U. Synaptic connectivity in the midget-parvocellular pathway of primate central retina. J Comp Neurol. 2006;494(2):260–74.
58. Smith VC, Lee BB, Pokorny J, Martin PR, Valberg A. Responses of macaque ganglion cells to the relative phase of heterochromatically modulated lights. J Physiol. 1992;458:191–221.
59. Lee BB, Kremers J, Yeh T. Receptive fields of primate retinal ganglion cells studied with a novel technique. Vis Neurosci. 1998;15(1):161–75.
60. Martin PR, Lee BB, White AJ, Solomon SG, Ruttiger L. Chromatic sensitivity of ganglion cells in the peripheral primate retina. Nature. 2001;410(6831):933–6.
61. Reid RC, Shapley RM. Space and time maps of cone photoreceptor signals in macaque lateral geniculate nucleus. J Neurosci. 2002;22(14):6158–75.
62. De Monasterio FM, Gouras P. Functional properties of ganglion cells of the rhesus monkey retina. J Physiol. 1975;251(1):167–95.
63. Lankheet MJ, Lennie P, Krauskopf J. Distinctive characteristics of subclasses of red-green P-cells in LGN of macaque. Vis Neurosci. 1998;15(1):37–46.
64. Diller L, Packer OS, Verweij J, McMahon MJ, Williams DR, Dacey DM. L and M cone contributions to the midget and parasol ganglion cell receptive fields of macaque monkey retina. J Neurosci. 2004;24(5):1079–88.
65. Buzas P, Blessing EM, Szmajda BA, Martin PR. Specificity of M and L cone inputs to receptive fields in the parvocellular pathway: random wiring with functional bias. J Neurosci. 2006;26(43):11148–61.
66. Silveira LC, Perry VH. The topography of magnocellular projecting ganglion cells (M-ganglion cells) in the primate retina. Neuroscience. 1991;40(1):217–37.
67. Grunert U, Greferath U, Boycott BB, Wassle H. Parasol (P alpha) ganglion-cells of the primate fovea: immunocytochemical staining with antibodies against GABAA-receptors. Vis Res. 1993;33(1):1–14.
68. Roorda A, Metha AB, Lennie P, Williams DR. Packing arrangement of the three cone classes in primate retina. Vis Res. 2001;41(10–11):1291–306.
69. Hofer H, Carroll J, Neitz J, Neitz M, Williams DR. Organization of the human trichromatic cone mosaic. J Neurosci. 2005;25(42):9669–79.
70. Neitz M, Balding SD, McMahon C, Sjoberg SA, Neitz J. Topography of long- and middle-wavelength sensitive cone opsin gene expression in human and Old World monkey retina. Vis Neurosci. 2006;23(3–4):379–85.
71. Cicerone CM, Nerger JL. The relative numbers of long-wavelength-sensitive to middle-wavelength-sensitive cones in the human fovea centralis. Vis Res. 1989;29(1):115–28.
72. Vimal RL, Pokorny J, Smith VC, Shevell SK. Foveal cone thresholds. Vis Res. 1989;29(1):61–78.
73. Wesner MF, Pokorny J, Shevell SK, Smith VC. Foveal cone detection statistics in color-normals and dichromats. Vis Res. 1991;31(6):1021–37.
74. Tuten WS, Harmening WM, Sabesan R, Roorda A, Sincich LC. Spatiochromatic interactions between individual cone photoreceptors in the human retina. J Neurosci. 2017;37(39):9498–509.

75. Greene MJ, Boehm AE, Vanston JE, Pandiyan VP, Sabesan R, Tuten WS. Unique yellow shifts for small and brief stimuli in the central retina. J Vis. 2024;24(6):2.
76. Krauskopf J. Color appearance of small stimuli and the spatial distribution of color receptors. J Opt Soc Am. 1964;54:1171.
77. Krauskopf J, Srebro R. Spectral sensitivity of color mechanisms: derivation from fluctuations of color appearance near threshold. Science. 1965;150(3702):1477–9.
78. Hofer H, Singer B, Williams DR. Different sensations from cones with the same photopigment. J Vis. 2005;5(5):444–54.
79. Koenig DE, Hofer HJ. Do color appearance judgments interfere with detection of small threshold stimuli? J Opt Soc Am A Opt Image Sci Vis. 2012;29(2):A258–67.
80. Domdei N, Reiniger JL, Holz FG, Harmening WM. The relationship between visual sensitivity and eccentricity, cone density and outer segment length in the Human Foveola. Invest Ophthalmol Vis Sci. 2021;62(9):31.
81. Vanston JE, Boehm AE, Tuten WS, Roorda A. It's not easy seeing green: the veridical perception of small spots. J Vis. 2023;23(5):2.
82. Gowdy PD, Cicerone CM. The spatial arrangement of the L and M cones in the central fovea of the living human eye. Vis Res. 1998;38(17):2575–89.
83. Witten JL, Lukyanova V, Harmening WM. Sub-cone visual resolution by active, adaptive sampling in the human foveola. elife. 2024;13:RP98648.
84. Brainard DH, Williams DR, Hofer H. Trichromatic reconstruction from the interleaved cone mosaic: Bayesian model and the color appearance of small spots. J Vis. 2008;8(5):15.
85. Domdei N, Linden M, Reiniger JL, Holz FG, Harmening WM. Eye tracking-based estimation and compensation of chromatic offsets for multi-wavelength retinal microstimulation with foveal cone precision. Biomed Opt Express. 2019;10(8):4126–41.
86. Lennie P, Haake PW, Williams DR. The design of chromatically opponent receptive fields. In: Landy MS, Movshon JA, editors. Computational modeling of visual processing. Cambridge: MIT Press; 1991. p. 71–82.
87. Forte JD, Blessing EM, Buzas P, Martin PR. Contribution of chromatic aberrations to color signals in the primate visual system. J Vis. 2006;6(2):97–105.
88. Hofer H, Williams DR. Color vision and the retinal mosaic. In: Werner JS, Chalupa LM, editors. The new visual neurosciences. Cambridge: MIT Press; 2014. p. 469–83.
89. Jacobs GH, Neitz J, Krogh K. Electroretinogram flicker photometry and its applications. J Opt Soc Am A Opt Image Sci Vis. 1996;13(3):641–8.
90. He J, Taveras Cruz Y, Eskew RT Jr. Methods for determining equiluminance in terms of L/M cone ratios. J Vis. 2020;20(4):22.
91. Brainard DH, Roorda A, Yamauchi Y, Calderone JB, Metha A, Neitz M, Neitz J, Williams DR, Jacobs GH. Functional consequences of the relative numbers of L and M cones. J Opt Soc Am A Opt Image Sci Vis. 2000;17(3):607–14.
92. Carroll J, McMahon C, Neitz M, Neitz J. Flicker-photometric electroretinogram estimates of L:M cone photoreceptor ratio in men with photopigment spectra derived from genetics. J Opt Soc Am A Opt Image Sci Vis. 2000;17(3):499–509.
93. Carroll J, Neitz J, Neitz M. Estimates of L:M cone ratio from ERG flicker photometry and genetics. J Vis. 2002;2(8):531–42.
94. Euler T, Haverkamp S, Schubert T, Baden T. Retinal bipolar cells: elementary building blocks of vision. Nat Rev Neurosci. 2014;15(8):507–19.
95. Thoreson WB, Mangel SC. Lateral interactions in the outer retina. Prog Retin Eye Res. 2012;31(5):407–41.
96. Lee BB, Martin PR, Grunert U. Retinal connectivity and primate vision. Prog Retin Eye Res. 2010;29(6):622–39.
97. Chichilnisky EJ, Baylor DA. Receptive-field microstructure of blue-yellow ganglion cells in primate retina. Nat Neurosci. 1999;2(10):889–93.

98. Field GD, Gauthier JL, Sher A, Greschner M, Machado TA, Jepson LH, Shlens J, Gunning DE, Mathieson K, Dabrowski W, Paninski L, Litke AM, Chichilnisky EJ. Functional connectivity in the retina at the resolution of photoreceptors. Nature. 2010;467(7316):673–7.
99. Li PH, Field GD, Greschner M, Ahn D, Gunning DE, Mathieson K, Sher A, Litke AM, Chichilnisky EJ. Retinal representation of the elementary visual signal. Neuron. 2014;81(1):130–9.
100. Kling A, Field GD, Brainard DH, Chichilnisky EJ. Probing computation in the primate visual system at single-cone resolution. Annu Rev Neurosci. 2019;42:169–86.
101. Dacey DM, Crook JD, Packer OS. Distinct synaptic mechanisms create parallel S-ON and S-OFF color opponent pathways in the primate retina. Vis Neurosci. 2014;31(2):139–51.
102. Gogliettino AR, Madugula SS, Grosberg LE, Vilkhu RS, Brown J, Nguyen H, Kling A, Hottowy P, Dabrowski W, Sher A, Litke AM, Chichilnisky EJ. High-fidelity reproduction of visual signals by electrical stimulation in the central primate retina. J Neurosci. 2023;43(25):4625–41.
103. Bouma BE, de Boer JF, Huang D, Jang IK, Yonetsu T, Leggett CL, Leitgeb R, Sampson DD, Suter M, Vakoc B, Villiger M, Wojtkowski M. Optical coherence tomography. Nat Rev Methods Primers. 2022:2.
104. Choma MA, Hsu K, Izatt JA. Swept source optical coherence tomography using an all-fiber 1300-nm ring laser source. J Biomed Opt. 2005;10(4):44009.
105. Ling T, Boyle KC, Zuckerman V, Flores T, Ramakrishnan C, Deisseroth K, Palanker D. High-speed interferometric imaging reveals dynamics of neuronal deformation during the action potential. Proc Natl Acad Sci USA. 2020;117(19):10278–85.
106. Pandiyan VP, Maloney-Bertelli A, Kuchenbecker JA, Boyle KC, Ling T, Chen ZC, Park BH, Roorda A, Palanker D, Sabesan R. The optoretinogram reveals the primary steps of phototransduction in the living human eye. Sci Adv. 2020;6(37)
107. Pandiyan VP, Nguyen PT, Pugh EN Jr, Sabesan R. Human cone elongation responses can be explained by photoactivated cone opsin and membrane swelling and osmotic response to phosphate produced by RGS9-catalyzed GTPase. Proc Natl Acad Sci USA. 2022;119(39):e2202485119.
108. Akkin T, Dave D, Milner T, Rylander Iii H. Detection of neural activity using phase-sensitive optical low-coherence reflectometry. Opt Express. 2004;12(11):2377–86.
109. Zhao YB, Yao XC. Intrinsic optical imaging of stimulus-modulated physiological responses in amphibian retina. Opt Lett. 2008;33(4):342–4.
110. Zhang P, Zawadzki RJ, Goswami M, Nguyen PT, Yarov-Yarovoy V, Burns ME, Pugh EN Jr. In vivo optophysiology reveals that G-protein activation triggers osmotic swelling and increased light scattering of rod photoreceptors. Proc Natl Acad Sci U S A. 2017;114(14):E2937–46.
111. Hillmann D, Spahr H, Pfaffle C, Sudkamp H, Franke G, Huttmann G. In vivo optical imaging of physiological responses to photostimulation in human photoreceptors. Proc Natl Acad Sci USA. 2016;113(46):13138–43.
112. Pandiyan VP, Jiang X, Maloney-Bertelli A, Kuchenbecker JA, Sharma U, Sabesan R. High-speed adaptive optics line-scan OCT for cellular-resolution optoretinography. Biomed Opt Express. 2020;11(9):5274–96.
113. Zhang F, Kurokawa K, Lassoued A, Crowell JA, Miller DT. Cone photoreceptor classification in the living human eye from photostimulation-induced phase dynamics. Proc Natl Acad Sci USA. 2019;116(16):7951–6.
114. Pandiyan VP, Schleufer S, Slezak E, Fong J, Upadhyay R, Roorda A, Ng R, Sabesan R. Characterizing cone spectral classification by optoretinography. Biomed Opt Express. 2022;13(12):6574–94.
115. Lassoued A, Zhang F, Kurokawa K, Liu Y, Bernucci MT, Crowell JA, Miller DT. Cone photoreceptor dysfunction in retinitis pigmentosa revealed by optoretinography. Proc Natl Acad Sci USA. 2021;118(47)
116. Tomczewski S, Curatolo A, Foik A, Wegrzyn P, Balamut B, Wielgo M, Kulesza W, Galinska A, Kordecka K, Gulati S, Fernandes H, Palczewski K, Wojtkowski M. Photopic flicker

optoretinography captures the light-driven length modulation of photoreceptors during phototransduction. Proc Natl Acad Sci USA. 2025;122(7):e2421722122.
117. Jonnal RS, Rha J, Zhang Y, Cense B, Gao W, Miller DT. In vivo functional imaging of human cone photoreceptors. Opt Express. 2007;15(4):16141–60.
118. Grieve K, Roorda A. Intrinsic signals from human cone photoreceptors. Invest Ophthalmol Vis Sci. 2008;49(2):713–9.
119. Bedggood P, Metha A. Variability in bleach kinetics and amount of photopigment between individual foveal cones. Invest Ophthalmol Vis Sci. 2012;53(7):3673–81.
120. Cooper RF, Tuten WS, Dubra A, Brainard DH, Morgan JIW. Non-invasive assessment of human cone photoreceptor function. Biomed Opt Express. 2017;8(11):5098–112.
121. Cooper RF, Brainard DH, Morgan JIW. Optoretinography of individual human cone photoreceptors. Opt Express. 2020;28(26):39326–39.
122. Domdei N, Ameln J, Gutnikov A, Witten JL, Holz FG, Wahl S, Harmening WM. Cone density is correlated to outer segment length and retinal thickness in the Human Foveola. Invest Ophthalmol Vis Sci. 2023;64(15):11.
123. Rolfs M. Microsaccades: small steps on a long way. Vis Res. 2009;49(20):2415–41.
124. Rucci M, Poletti M. Control and functions of fixational eye movements. Annu Rev Vis Sci. 2015;1:499–518.
125. Schnapf JL, Nunn BJ, Meister M, Baylor DA. Visual transduction in cones of the monkey Macaca fascicularis. J Physiol. 1990;427:681–713.
126. Cao LH, Luo DG, Yau KW. Light responses of primate and other mammalian cones. Proc Natl Acad Sci USA. 2014;111(7):2752–7.
127. Linsenmeier RA, Hertz BG. Eye movements in paralyzed cats induced by drugs and sympathetic stimulation. Vis Res. 1979;19(11):1249–52.
128. Forte J, Peirce JW, Kraft JM, Krauskopf J, Lennie P. Residual eye-movements in macaque and their effects on visual responses of neurons. Vis Neurosci. 2002;19(1):31–8.
129. Sincich LC, Zhang Y, Tiruveedhula P, Horton JC, Roorda A. Resolving single cone inputs to visual receptive fields. Nat Neurosci. 2009;12(8):967–9.
130. Hofer H, Artal P, Singer B, Aragon JL, Williams DR. Dynamics of the eye's wave aberration. J Opt Soc Am A Opt Image Sci Vis. 2001;18(3):497–506.
131. Dubra A, Sulai Y, Norris JL, Cooper RF, Dubis AM, Williams DR, Carroll J. Noninvasive imaging of the human rod photoreceptor mosaic using a confocal adaptive optics scanning ophthalmoscope. Biomed Opt Express. 2011;2(7):1864–76.
132. Marcos S, Werner JS, Burns SA, Merigan WH, Artal P, Atchison DA, Hampson KM, Legras R, Lundstrom L, Yoon G, Carroll J, Choi SS, Doble N, Dubis AM, Dubra A, Elsner A, Jonnal R, Miller DT, Paques M, Smithson HE, Young LK, Zhang Y, Campbell M, Hunter J, Metha A, Palczewska G, Schallek J, Sincich LC. Vision science and adaptive optics, the state of the field. Vis Res. 2017;132:3–33.
133. Thibos LN, Bradley A, Still DL, Zhang X, Howarth PA. Theory and measurement of ocular chromatic aberration. Vis Res. 1990;30(1):33–49.
134. Atchison DA, Smith G. Chromatic dispersions of the ocular media of human eyes. J Opt Soc Am A Opt Image Sci Vis. 2005;22(1):29–37.
135. Vinas M, Dorronsoro C, Cortes D, Pascual D, Marcos S. Longitudinal chromatic aberration of the human eye in the visible and near infrared from wavefront sensing, double-pass and psychophysics. Biomed Opt Express. 2015;6(3):948–62.
136. Harmening WM, Tiruveedhula P, Roorda A, Sincich LC. Measurement and correction of transverse chromatic offsets for multi-wavelength retinal microscopy in the living eye. Biomed Opt Express. 2012;3(9):2066–77.
137. Simonet P, Campbell MC. The optical transverse chromatic aberration on the fovea of the human eye. Vis Res. 1990;30(2):187–206.
138. Winter S, Sabesan R, Tiruveedhula P, Privitera C, Unsbo P, Lundstrom L, Roorda A. Transverse chromatic aberration across the visual field of the human eye. J Vis. 2016;16(14):9.

139. Rynders M, Lidkea B, Chisholm W, Thibos LN. Statistical distribution of foveal transverse chromatic aberration, pupil centration, and angle psi in a population of young adult eyes. J Opt Soc Am A Opt Image Sci Vis. 1995;12(10):2348–57.
140. Marcos S, Burns SA, Prieto PM, Navarro R, Baraibar B. Investigating sources of variability of monochromatic and transverse chromatic aberrations across eyes. Vis Res. 2001;41(28):3861–71.
141. Aissati S, Vinas M, Benedi-Garcia C, Dorronsoro C, Marcos S. Testing the effect of ocular aberrations in the perceived transverse chromatic aberration. Biomed Opt Express. 2020;11(8):4052–68.
142. Roorda A, Cholewiak SA, Bhargava S, Ivzan NH, LaRocca F, Nankivil D, Banks MS. The visual benefits of correcting longitudinal and transverse chromatic aberration. J Vis. 2023;23(2):3.
143. Westheimer G, McKee SP. Spatial configurations for visual hyperacuity. Vis Res. 1977;17(8):941–7.
144. Marcos S, Burns SA, Moreno-Barriusop E, Navarro R. A new approach to the study of ocular chromatic aberrations. Vis Res. 1999;39(26):4309–23.
145. Boehm AE, Privitera CM, Schmidt BP, Roorda A. Transverse chromatic offsets with pupil displacements in the human eye: sources of variability and methods for real-time correction. Biomed Opt Express. 2019;10(4):1691–706.
146. Snodderly DM, Weinhaus RS, Choi JC. Neural-vascular relationships in central retina of macaque monkeys (Macaca fascicularis). J Neurosci. 1992;12(4):1169–93.
147. Yu DY, Cringle SJ, Yu PK, Balaratnasingam C, Mehnert A, Sarunic MV, An D, Su EN. Retinal capillary perfusion: spatial and temporal heterogeneity. Prog Retin Eye Res. 2019;70:23–54.
148. Burns SA, Elsner AE, Gast TJ. Imaging the retinal vasculature. Annu Rev Vis Sci. 2021;7:129–53.
149. Bedggood P, Metha A. Adaptive optics imaging of the retinal microvasculature. Clin Exp Optom. 2020;103(1):112–22.
150. Schiefer U, Benda N, Dietrich TJ, Selig B, Hofmann C, Schiller J. Angioscotoma detection with fundus-oriented perimetry. A study with dark and bright stimuli of different sizes. Vis Res. 1999;39(10):1897–909.
151. Remky A, Beausencourt E, Elsner AE. Angioscotometry with the scanning laser ophthalmoscope. Comparison of the effect of different wavelengths. Invest Ophthalmol Vis Sci. 1996;37(11):2350–5.
152. Adams DL, Horton JC. Shadows cast by retinal blood vessels mapped in primary visual cortex. Science. 2002;298(5593):572–6.
153. Adams DL, Horton JC. A precise retinotopic map of primate striate cortex generated from the representation of angioscotomas. J Neurosci. 2003;23(9):3771–89.
154. Tuten WS, Tiruveedhula P, Roorda A. Adaptive optics scanning laser ophthalmoscope-based microperimetry. Optom Vis Sci. 2012;89(5):563–74.
155. Nishiwaki H, Ogura Y, Kimura H, Kiryu J, Miyamoto K, Matsuda N. Visualization and quantitative analysis of leukocyte dynamics in retinal microcirculation of rats. Invest Ophthalmol Vis Sci. 1996;37(7):1341–7.
156. Tam J, Tiruveedhula P, Roorda A. Characterization of single-file flow through human retinal parafoveal capillaries using an adaptive optics scanning laser ophthalmoscope. Biomed Opt Express. 2011;2(4):781–93.
157. Uji A, Hangai M, Ooto S, Takayama K, Arakawa N, Imamura H, Nozato K, Yoshimura N. The source of moving particles in parafoveal capillaries detected by adaptive optics scanning laser ophthalmoscopy. Invest Ophthalmol Vis Sci. 2012;53(1):171–8.
158. Roorda A, Williams DR. Optical fiber properties of individual human cones. J Vis. 2002;2(5):404–12.
159. Sinclair SH, Azar-Cavanagh M, Soper KA, Tuma RF, Mayrovitz HN. Investigation of the source of the blue field entoptic phenomenon. Invest Ophthalmol Vis Sci. 1989;30(4):668–73.

160. Martin JA, Roorda A. Direct and noninvasive assessment of parafoveal capillary leukocyte velocity. Ophthalmology. 2005;112(12):2219–24.
161. Martin JA, Roorda A. Pulsatility of parafoveal capillary leukocytes. Exp Eye Res. 2009;88(3):356–60.
162. Tam J, Martin JA, Roorda A. Noninvasive visualization and analysis of parafoveal capillaries in humans. Invest Ophthalmol Vis Sci. 2010;51(3):1691–8.
163. Bruce KS, Harmening WM, Langston BR, Tuten WS, Roorda A, Sincich LC. Normal perceptual sensitivity arising from weakly reflective cone photoreceptors. Invest Ophthalmol Vis Sci. 2015;56(8):4431–8.
164. Guevara-Torres A, Joseph A, Schallek JB. Label free measurement of retinal blood cell flux, velocity, hematocrit and capillary width in the living mouse eye. Biomed Opt Express. 2016;7(10):4228–49.
165. Ashbery D, Baez HC, Kanarr RE, Kunala K, Power D, Chu CJ, Schallek J, McGregor JE. In vivo visualization of intravascular patrolling immune cells in the primate eye. Invest Ophthalmol Vis Sci. 2024;65(11):23.
166. Neriyanuri S, Bedggood P, Symons RCA, Metha AB. Flow heterogeneity and factors contributing to the variability in retinal capillary blood flow. Invest Ophthalmol Vis Sci. 2023;64(10):15.
167. Harmening WM, Tuten WS, Roorda A, Sincich LC. Mapping the perceptual grain of the human retina. J Neurosci. 2014;34(16):5667–77.
168. Arathorn DW, Yang Q, Vogel CR, Zhang Y, Tiruveedhula P, Roorda A. Retinally stabilized cone-targeted stimulus delivery. Opt Express. 2007;15(21):13731–44.
169. Yang Q, Arathorn DW, Tiruveedhula P, Vogel CR, Roorda A. Design of an integrated hardware interface for AOSLO image capture and cone-targeted stimulus delivery. Opt Express. 2010;18(17):17841–58.
170. Wilson ME. Invariant features of spatial summation with changing locus in the visual field. J Physiol. 1970;207(3):611–22.
171. Lie I. Visual detection and resolution as a function of retinal locus. Vis Res. 1980;20(11): 967–74.
172. Anderson SJ, Mullen KT, Hess RF. Human peripheral spatial resolution for achromatic and chromatic stimuli: limits imposed by optical and retinal factors. J Physiol. 1991;442:47–64.
173. Volbrecht VJ, Shrago EE, Schefrin BE, Werner JS. Spatial summation in human cone mechanisms from 0 degrees to 20 degrees in the superior retina. J Opt Soc Am A Opt Image Sci Vis. 2000;17(3):641–50.
174. Drasdo N, Millican CL, Katholi CR, Curcio CA. The length of Henle fibers in the human retina and a model of ganglion receptive field density in the visual field. Vis Res. 2007;47(22):2901–11.
175. Bruce KS. Elementary photoreceptor signaling in human vision. In: Department of Optometry and Vision Science. University of Alabama at Birmingham; 2016. p. 1–189.
176. Nerger JL, Cicerone CM. The ratio of L cones to M cones in the human parafoveal retina. Vis Res. 1992;32(5):879–88.
177. Otake S, Cicerone CM. L and M cone relative numerosity and red-green opponency from fovea to midperiphery in the human retina. J Opt Soc Am A Opt Image Sci Vis. 2000;17(3):615–27.
178. Williams DR, MacLeod DI, Hayhoe MM. Punctate sensitivity of the blue-sensitive mechanism. Vis Res. 1981;21(9):1357–75.
179. Makous W, Carroll J, Wolfing JI, Lin J, Christie N, Williams DR. Retinal microscotomas revealed with adaptive-optics microflashes. Invest Ophthalmol Vis Sci. 2006;47(9):4160–7.
180. Morgan JIW, Chui TYP, Grieve K. Twenty-five years of clinical applications using adaptive optics ophthalmoscopy [invited]. Biomed Opt Express. 2023;14(1):387–428.
181. Foote KG, Loumou P, Griffin S, Qin J, Ratnam K, Porco TC, Roorda A, Duncan JL. Relationship between foveal cone structure and visual acuity measured with adaptive optics scanning laser ophthalmoscopy in retinal degeneration. Invest Ophthalmol Vis Sci. 2018;59(8):3385–93.

182. Tu JH, Foote KG, Lujan BJ, Ratnam K, Qin J, Gorin MB, Cunningham ET Jr, Tuten WS, Duncan JL, Roorda A. Dysflective cones: visual function and cone reflectivity in long-term follow-up of acute bilateral foveolitis. Am J Ophthalmol Case Rep. 2017;7:14–9.
183. Wang Q, Tuten WS, Lujan BJ, Holland J, Bernstein PS, Schwartz SD, Duncan JL, Roorda A. Adaptive optics microperimetry and OCT images show preserved function and recovery of cone visibility in macular telangiectasia type 2 retinal lesions. Invest Ophthalmol Vis Sci. 2015;56(2):778–86.
184. Duncan JL, Roorda A. Dysflective cones. Adv Exp Med Biol. 2019;1185:133–7.
185. Bensinger E, Wang Y, Roorda A. Patches of dysflective cones in eyes with no known disease. Invest Ophthalmol Vis Sci. 2022;63(1):29.
186. Yeh T, Smith VC, Pokorny J. The effect of background luminance on cone sensitivity functions. Invest Ophthalmol Vis Sci. 1989;30(10):2077–86.
187. Cole GR, Hine T. Computation of cone contrasts for color vision research. Behav Res Meth Inst Comp. 1992;24:22–7.
188. DeVries SH, Qi X, Smith R, Makous W, Sterling P. Electrical coupling between mammalian cones. Curr Biol. 2002;12(22):1900–7.
189. Hornstein EP, Verweij J, Schnapf JL. Electrical coupling between red and green cones in primate retina. Nat Neurosci. 2004;7(7):745–50.
190. Tuten WS, Harmening WM, Sabesan R, Sincich LC, Roorda A. Functional mapping of the trichromatic cone mosaic in vivo. In: Fall vision meeting abstracts. Philadelphia: Optical Society of America; 2014.
191. Cohen J. Weighted kappa: nominal scale agreement with provision for scaled disagreement or partial credit. Psychol Bull. 1968;70(4):213–20.
192. Sabesan R, Tuten WS, Roorda A. Mapping the human trichromatic cone mosaic with an AOSLO. In: ARVO; 2014.
193. Sabesan R, Schmidt BP, Tuten WS, Roorda A. The elementary representation of spatial and color vision in the human retina. Sci Adv. 2016;2(9):e1600797.
194. Schmidt BP, Boehm AE, Tuten WS, Roorda A. Spatial summation of individual cones in human color vision. PLoS One. 2019;14(7):e0211397.
195. Fong J, Doyle HK, Wang C, Boehm AE, Herbeck SR, Pandiyan VP, Schmidt BP, Tiruveedhula P, Vanston JE, Tuten WS, Sabesan R, Roorda A, Ng R. Novel color via stimulation of individual photoreceptors at population scale. Sci Adv. 2025;11(16):eadu1052.
196. van den Berg TJ, Franssen L, Kruijt B, Coppens JE. History of ocular straylight measurement: a review. Z Med Phys. 2013;23(1):6–20.
197. Meadway A, Sincich LC. Light propagation and capture in cone photoreceptors. Biomed Opt Express. 2018;9(11):5543–65.